MAX-PLANCK-INSTITUT FÜR PLASMAPHYSIK

GARCHING BEI MÜNCHEN

Edge Density Measurements with a Fast Li-Beam
Probe on Tokamak and Stellarator Experiments

K. McCormick, S. Fiedler, G. Kocsis,
J. Schweinzer and S. Zoletnik

IPPIII/211   March 1996

Edge Density Measurements with a Fast Li-Beam Probe

on Tokamak and Stellarator Experiments

K. McCormick[1], S. Fiedler[1], G. Kocsis[2], J. Schweinzer[1] and S. Zoletnik[2]

(1) Max-Planck-Institut für Plasmaphysik, EURATOM Association, 85748 Garching, Germany

(2) KFKI-Research Inst., Dept. of Plasma Physics, P.O.Box 49, Budapest-114, Hungary

Abstract

High-energy neutral Li-beam probes have advanced to the point where they are a standard diagnostic on W7-AS and ASDEX-Upgrade, both in terms of the Li-beam injector and the reconstruction algorithm to arrive at densities along the beam $n_e(z)$ from the Li[2p-2s] resonance line profile. With beam energies in the range 30-70 keV and neutral equivalent currents of >1mA, it is possible to produce $n_e(z)$ profiles for line densities $\overline{n_e z} < 4 \times 10^{14}$ cm^{-2} with a radial resolution of ~ 0.5 cm and time response $\leq$ 0.2msec. The IPP Li-gun is described. By way of example, the diagnostic layout on W7-AS is sketched and salient results from experiment presented which serve to explore diagnostic limits and to underline the viability of the technique. Densities over the range <10^{12} - 10^{14} cm^{-3} are accessible, permitting full coverage of the core density gradient region on W7-AS. Examples from ASDEX involving the H-mode and pellet injection are presented to exemplify time response. Scaling of SOL density e-folding lengths are introduced to point out possible differences between tokamak (ASDEX, ASDEX-Up) and stellarator (W7-AS) transport behavior perpendicular to field lines.

A neutral lithium beam can also be employed to measure (a) impurity ion temperatures and densities via CXRS, and (b) neutral pressure outside the plasma column /1/. These aspects lie outside the scope of the present paper.

1. Introduction

Knowledge of the temporal and spatial behavior of edge/SOL density profiles on fusion-oriented experiments is a prerequisite for many facets of investigation. Validation of transport codes and deduction of transport coefficients relies heavily on exact experimental results being available over a wide range of conditions - spanning, for example, ELM-free H-modes to the case of impurity-seeded high recycling/detached divertors. Experimental verification of the approach of edge pressure gradients to instability limits requires $n_e(r)$ as one of its elements. The design of divertor entrance baffles aimed at controlling neutral back flow

depends on getting the balance right between allowing most of the plasma to enter, which is a function of the SOL T_e- and n_e-profiles, and restriction of the neutral flow back into the main chamber from the divertor region. The coupling of ICRH power to the plasma is a sensitive function of the SOL density profile, awareness of which can help to understand ICRH behavior. The existence of edge structures such as islands is directly reflected in $n_e(r)$ /2/, and in the same way one may hope to be able to identify 2D coherent structures (eddies) associated with turbulent transport in the edge/SOL /3/.

A Li- beam probe is non-perturbing and thus is not subject to restrictions concerning the plasma conditions under which it can be used - unlike, for example, Langmuir probes. Its result is also not disturbed by non-thermal electron distributions or density fluctuations, and can even be used as a fluctuation diagnostic in the region of moderate beam attenuation /3, 4/.

Proof-of-principle experiments were initially carried out on a low-density test plasma using a 4kV/10μA beam and synchronous detection techniques /5/. The first routine application to a fusion-relevant plasma was on ASDEX with beam properties of 60kV/0.6mA /6, 7/. Below, after discussing the principles of the diagnostic in section 2, properties of the neutral lithium beam gun developed at the IPP/Garching are detailed along with the optical detection scheme of W7-AS, followed by a variety of experimental results from ASDEX, ASDEX-Upgrade and W7-AS to illustrate the scope of the method at the present time.

2. Principles

By observing the resonance line radiation profile emitted from an alkali neutral beam as it traverses a plasma it is possible to deduce the density profile $n_e(z)$. The necessary reconstruction technique depends principally on the beam energy : Thermal beams as a result of their low velocity are dominated by electron interactions. They attenuate rapidly, hence even at the upper end of their practical useful range (about 5×10^{12} cm^{-3} /8, 9/) very simple models suffice to arrive at a density profile. Higher energy beams suffer less attenuation and thus penetrate into regions of high density where multi-step processes within the beam atom become relevant. Reconstruction demands a full collisional-radiative model considering electrons as well as excitation/ionization/charge-exchange by all plasma ions. Such models exist /10, 11/. The technique developed at the IPP /10/, inherently capable of deriving absolute

$n_e(z)$ profiles from the relative line radiation profile without need of cross-calibration, is used in this paper. $T_e(z)$ and $Z_{eff}(z)$ influence the derived $n_e(z)$ only weakly, so no more than reasonable estimates of each are necessary, as will be shown in section 4 below. Nonetheless, a reliable cross section database for protons and impurity ions as well as electrons (extending into the n=4 level of Li^0 for high density evaluation) is vitally necessary in order to make such statements and has only recently become available /12-14/.

The probing beam atom should have (1) a low molecular mass in order to attain the necessary velocities at comfortable beam energies, (2) the resonance line should lie in the visible range so as to allow simple optics and high photon detection efficiency, (3) preferably the line should lie in a quiet part of the spectrum, and (4) the lifetime τ of the resonance line excited state should be small to minimize the product of beam velocity v_b and τ, thereby localizing the excitation-emission process. Lithium does not satisfy the fourth point particularly well (at 60keV, $\tau v_b = 3.5cm$), nevertheless experience indicates that for profiles typically encountered at the edge this is not a limitation, and can be adequately accounted for within the reconstruction algorithm.

Ideally, the probing beam will be injected into the plasma perpendicular to flux surfaces to optimize penetration and should be viewed tangentially to flux surfaces to optimize radial resolution. A small beam diameter will boost the signal/background ratio and promote radial resolution where these injection/viewing conditions cannot be fully met.

3. Experimental Apparatus

The original motivation for development of a Li-beam gun at the IPP/Garching was to measure the tokamak current density distribution via the Zeeman effect /15/. Whereas the technique was used with success on Pulsator at densities $\overline{n_e} \leq 4\times10^{13}$ (plasma radius a = 10cm) /16/ and on ASDEX for $\overline{n_e} \leq 1\times10^{13}$ cm^{-3} (a = 40cm) /17/, it became clear that energies well in excess of 100 keV would be required to access higher densities. Thus, emphasis was shifted to $n_e(r)$ measurements at the plasma edge, with use of the same gun.

3.1.1 The IPP Ion Gun

To be acceptable as part of a standard diagnostic, the ion gun must not only produce a high-quality beam, it should do this over a long lifetime with a degree of robustness and reliability

such as to virtually eliminate daily servicing and fine-tuning. Employment of the lithium resonance line, as opposed to light originating from higher state transitions, translates into a high beam brightness via collisional excitation, and therefore permits use of a relatively low beam current. The lithium aluminosilicate, ß-eucryptite ($Li_2O \cdot Al_2O_3 \cdot 2SiO_2$), is the ideal source in terms of simplicity - it need only be heated to near 1300 ^oC and an electric field applied to extract lithium ion currents in the mA/cm^2 range. Further, the low temperature yields a low transverse ion temperature, which augments the beam focusing capability.

Fig. 1 depicts the ion gun originally installed on ASDEX and which continues service on W7-AS in an improved form. The emitter (a specially-developed commercial unit from Spectra Mat. in Calif. /18/) consists of a porous tungsten plug base of nominal 15mm diameter which is resistively heated at about 32A/7VAC to attain the temperature needed for copious Li^+ emission from the ~0.1g ß-eucryptite coating. With a 60kV difference between the two-tube immersion lens, application of V_{ex} = 9.4kV between extractor and emitter (of Pierce design) yields an ion current ≤ 5mA which after acceleration to V_b = 69.4kV and focusing passes through the sodium vapor neutralizer to form a 3mA neutral beam of about 10mm FWHM at ~2.3m from the neutralizer housing. On an experiment, the operational ratio of V_{ex}/V_b is determined by increasing V_{ex} in small (~100V) steps until the trade-off between increasing beam width and increasing beam current is optimized. Subsequently, reproducible beam properties are achieved by holding this ratio to better than 1%.

Experimentally it has been established that the neutral beam current may be varied according to the relationship I_b[mA equivalent] = 0.0096 $V_b^{1.36}$ (over V_b = 13-70kV, fig.3), while maintaining the ratio V_{ex}/V_b in order to preserve good beam quality. The number of lithium neutrals per cm of beam is then N_b ~ $3.6 \times 10^6 V_b^{0.86}$ or ~ 0.3 - 1.4 x 10^8 over 13 - 70kV.

The original ASDEX gun /19/ had a I_b-V_b characteristic of I_b = $7.6 \times 10^{-4} V_b^{1.65}$ (20-100kV), meaning the improved version is better by a ratio of 5.3 - 3.7 over 20-70kV. This was realized by increasing the bore of the grounded tube from 30 to 40mm and, through experimental optimization, adjusting the tube separation to 35mm and the emitter-extractor distance to 22mm, all of which permitted a well-focused beam to be achieved at a higher V_{ex}/V_b ratio, thereby yielding higher extracted currents. All distances are adjustable from outside, so it was straightforward to experimentally optimize gun properties once the tube diameter had been

enlarged. Beam calculations, taking into account the effect of space charge, nicely supported the experimental results /20/. Subsequent editions of the gun (on ASDEX-Upgrade /20, 21/, TEXTOR /22/ and JET /22/) use a fixed version of this optimized emitter-extractor-lens geometry with slight variations. Still simpler low current Li^o guns based on ß-eucryptite exist ($<$10kV/50µA) /23, 24, 25/, as well as the General Atomics development line using large emitters (now 30kV/5-10mA /3, 26/). Thermal Li^o sources, excellent for low-density work, are not considered here /9, 27/.

Years of experience on ASDEX indicate Li^+ ions stored in the ß-eucryptite are not lost by heating alone, but only in combination with an extracting field, in agreement with the literature /28-33/. At low emission currents ($<$1mA/cm^2) most ions can be removed from the ß-eucryptite lattice, leading to a mA-sec rating for a 0.1g coating of $\sim 8.6 \times 10^4$, or $\sim 10^4$ pulses of 4 sec length at 2mA. In practice some fraction of this number (on ASDEX, greater than 10%), even for high emission values, can be attained.

3.1.2 The IPP neutralizer

The neutralizer (fig.2), capable of operation in both vertical and horizontal positions, consists of a neutralization tube of 12cm length and 2.5 cm inner diameter, attached to a reservoir containing sodium /34/. The tube/reservoir are heated independently via coaxial heating cables, typically at 0.85/0.95A for powers of $\sim$17/65W. Variacs are used as power supplies with no regulation. The reservoir temperature is $\sim$240 ^{o}C, meaning the tube pressure is in the 10^{-3} mbar range for which sodium loss rates of $\sim$100µg/sec, or 1 gram in $<$ 3 hours are expected for the given geometry. To reduce cell losses, operation is on a pulsed basis by means of a valve which seals the reservoir when the beam in not on. Hence, a 1 gram loading of sodium should be lost in about 2000 shots of five seconds length. Practical experience on ASDEX is not inconsistent with this number. Sodium is used rather than lithium in order to have the convenience of running at lower temperatures (about 240 ^{o}C vs. 500 ^{o}C), and to avoid having thermal Li[2p] signals interfering with those from the high energy beam.

Based on calorimetric measurements, the neutralization efficiencies ε realized are $\sim$ 95 - 68% for 20 - 70kV, and can be approximately summarized in the fit $\varepsilon \sim 107 \, e^{-0.0065 \, V_b}$ (fig.3). Taking into account the decrease of ε with V_b, and the current $I_{emitter}$ drawn from the power

supply in conjunction with the neutral beam current scaling of above, it emerges that 81-90% (20-70kV) of I_e is utilized, i.e. only about 19-10% of the ions leaving the emitter are lost.

3.1.3 The Beam Line

For discrimination against background light the beam may be chopped mechanically (W7-AS: on/off times ~5/1 at ~16Hz), or electrostatically on a time scale in the µs range. Shielding the beam line against magnetic fields (up to 500G in the neutralizer plane on ASDEX) is accomplished by the vacuum vessel itself which is made of ARMCO iron coated with nickel.

3.2 Detection Systems

On W7-AS (fig.4) the optical system for determining $n_e(r)$ consists of an achromat ($\Omega/4\pi \sim 3 \times 10^{-4}$) of focal length 600mm, followed by a 3-period interference filter ($\lambda_o \sim 6724$Å, FWHM~24Å) and an f/2 135mm objective which images the beam on a set of 28 fiber bundles (70µ optical fiber of Schott A2 glass, equivalent bundle diameter ~2.4mm, length 5.5m) each coupled into either an R928 or R3896 Hamamatsu photomultiplier /1/. The image of the bundles, each rectangular in form, subtends either ~ 6mm (first 20 channels from the outside) or ~ 10mm along an ~ 20cm beam length from the far SOL to the plasma center.

The 24Å filter permits use of one filter overall instead of one filter per channel, making for a simple system, but the signal/background ratios at the extreme ends of the Li[2p] profile then often fall below one (see fig. 5). The width of 24Å is necessary in order to compensate for the Doppler shift along the viewing path and to permit a range of beam voltages for test purposes.

Photomultipliers are used as detectors to optimize signal/noise for lower-level signals as well as to permit density fluctuation measurements up to the 100kHz region. A relative calibration among the 28 optical-detector chains is achieved in situ by observing Li[2p] radiation emitted from the beam as it passes through the neutral gas in the torus after each discharge. For the gas pressures confronted (~10^{-4} mbar range) no significant beam attenuation over the 20cm optically interrogated path is to be expected. The linearity of the PM-amplifier chain is particularly important as the differences between Li[2p] amplitudes arising from plasma -beam or neutral-beam interactions (during calibration) may be more than 100. On W7-AS the analogue signal was initially filtered with an RC time constant of 0.2ms and digitized at 5kHz.

The simple RC filters have now been replaced by anti-aliasing active filters of the Bessel type with a variable cutoff frequency range extending to 50kHz.

It is worthwhile to mention detection systems elsewhere. TEXTOR reports it will use a 20Å interference filter in conjunction with a 256 photodiode camera array and an envisaged integration time window of 5 ms, using electrostatic beam chopping as on W7-AS/ASDEX-Upgrade to register the background /9/. JET uses a spectrometer/CCD camera layout which has a potential minimal integration time of 20 ms /35/. On JET, beam modulation to pick out the background is not necessary as this information can be inferred by spectrally interpolating between light intensities to the left and right of the lithium line. This system has the further advantage that, should intensities be adequate, Li-beam-activated CXRS on impurities can be performed as well with the same setup /36/.

4. Experimental Results

The Li[2p] light profile in fig.5a initially rises because of the increasing density, and then falls as beam attenuation begins to dominate. The ratio Li[2p]/background is poor as the beam enters the plasma, because of (a) the low density (see fig.5b), (b) the 24Å FWHM passband of the interference filter, and (c) the long viewing path through the plasma (see fig.4). Considering the statistical noise of the background and of the Li[2p] signal in conjunction with the ~ 1% error in the relative calibration of each channel, and then carrying out profile reconstruction on the associated statistical sets of Li[2p] profiles leads to a corresponding band of $n_e(z)$ profiles (fig.5b) to give a feeling for the absolute error of the method. Since the errors are progressive as the beam travels further into the plasma, the absolute error becomes larger with increasing z, but generally remains small on the ascending part of the Li[2p] profile.

4.1 Influence of beam energy, density T_e and Z_{eff} on the efficacy of the diagnostic

Beam penetration as a function of E_{beam} on W7-AS is examined in fig.6a where normalized Li[2p] profiles are plotted for E_{beam} = 20, 30, 48 and 66keV for identical discharge conditions. At the extreme end of the range there is a factor of about three difference between 20 and 66 keV, but the amount is less where reconstruction is possible (see fig.6b). Thus, from the standpoint of penetration, large factors cannot be gained in going to high energies, although there is still the additional advantage of higher beam currents. The reconstructed

profiles of fig. 6b for 30-66kV lie very close to each other, giving confidence the velocity dependence of the interaction cross sections is reasonably correct. The deviation of the 20kVprofile is due to a poor signal/background ratio rather than to improper cross sections.

The decrease in penetration depth (E_{beam}=48keV) with increasing density is studied in fig.7a where the Li[2p] profiles along the beam axis are given for four density steps carried out in one discharge. Higher densities lead to a progressive constriction of the measurement to the outside. Even so, the core gradient region is still fully accessed as is evident from the corresponding $n_e(z)$ profiles of fig.7b. Using these four profiles as a guide, the area under the curves indicates that density determinations are possible for an integrated line density along the beam path of $\overline{n_e z} \leq 4 \times 10^{14}$ cm^{-2}. Beam injection occurs in a region of highly compressed flux surfaces, allowing good measurements to the plasma center for $n_{eo} < 4 \times 10^{13}$ cm^{-3}. This compression also contributes to the steep density profiles at the edge, which change more than two orders of magnitude in only 4 cm.

Fig. 8 gives $n_e(R_{eff})$ profiles for another discharge over a density range similar to fig. 7, but for a density ramp instead of steady-state conditions. The difference in profile form and absolute magnitude between the last two time points (just before reduction of the gas puff, and the steady-state phase), which have about the same $\overline{n_e L}$, illustrates the profile peaking effect attendant upon reduction of the gas puff and underlines the necessity of careful consideration of discharge setup in carrying out studies of edge/SOL n_e-profiles.

At high beam energies the Li[2s-2p] excitation rates depend only weakly on T_e or T_{ion}, as shown in fig.9. Thus, it is to be expected that reconstructed $n_e(z)$ profiles will also depend weakly on $T_e(z)$. Referring to fig.10, using $T_e(z)$ from the high density case of fig.8 at t=0.5 sec to reconstruct the low density case at t=0.14 sec leads to a 10% underestimate in density, although the given $T_e(z)$ profiles lie more than a factor of two apart in the central region. Conversely, taking $T_e(z)$ from the low density case to deconvolve the high density profile leads to a non-perceptible error, as the beam largely extinguishes before the temperature differences become important. Nevertheless, if SOL temperatures begin to fall below 20eV, then the total excitation rate for 20keV, for example, of fig.9 changes more than a factor of two over T_e=20-1eV. In this case, an imprecise description of the T_e profile within the radiative-collisional model can lead to important errors in derivation of SOL falloff lengths.

A reasonable estimate of Z_{eff} suffices for the reconstruction algorithm. For exemplification, using $Z_{eff}(0) = 1.0$ instead of 2.5 in fig.11 leads to an increase of ~10% in $n_e(z)$ at $V_b = 60keV$. For a 30kV beam there is no visible change in the end result of fig.11 for $Z_{eff}(0) = 1-2.5$ /21/. Here, $Z_{eff}(0)$ ~2.5 is a reasonable estimate, for which the 30 and 60keV profiles closely agree, again demonstrating the consistency of atomic data sets used for reconstruction, as well as the basic low noise level and reproducibility of results of the Li-beam diagnostic.

Fig.12 compares density profile measurements derived from Thomson scattering, the Li-beam and a Langmuir probe, and fig.13 juxtaposes reflectometer and Li-beam profiles. All these diagnostics are situated at different toroidal positions, necessitating a coordinate transformation into R_{eff} space to permit an overlay. The agreement is excellent, in particular considering potential errors in the mapping process. For example, shifting the Li-profile in fig.12 by ~2mm in beam-coordinates would yield a perfect overlapping of the Li-Langmuir curves in the range R_{eff} ~18-21cm. Or, the same effect is achieved by increasing the Langmuir values by 25%. In any case, the lithium beam nicely covers the range from the far SOL to the core with a density spread of $4 \times 10^{11} - 6 \times 10^{13}$ cm^{-3}.

4.2 Examples Demonstrating Time Response

Several examples from ASDEX are now presented to illustrate the temporal capabilities of the diagnostic for various situations on a divertor tokamak. (ASDEX had 10 observation channels covering 10cm in the plasma periphery. /6, 7/) Fig.14a shows Li[2p] signals from a set of 5 neighboring channels approximately centered on the separatrix over a time span of 100ms during which three pellets have been injected /37/. Injection of the pellet is registered as a smooth increase in density over 2ms on the core channels (R_S-1, R_S-2) followed by a uniform decay until the next pellet. In the SOL the pellet produces a short perturbation followed by a rapid decrease of density, corresponding to a steepening of the SOL density falloff length. Thereafter the SOL profile relaxes back to the pre-pellet form. The 3D picture of fig.14b gives a good overview of events, attests to the low noise level of the signals, and illustrates the futility of attempting to meaningfully interrogate edge plasma profiles under such conditions with a diagnostic not capable of continuous measurements.

Fig. 15a shows a 3D plot of Li[2p] over 11 ms on ASDEX, but now spanning two ELM events during an ELMy H-mode phase /38/. The ELM rise is faster than the 200μs sampling interval, but the ELM decay over a few ms is fully registered, as an example of a reconstructed ELM density profile in fig.15b illustrates. The SOL density e-folding length λ_{ne} varies from about 4 to 1 cm over the decay time. Note in the 3D picture how the profiles return to the same form in between ELMs. This behavior is more completely documented in fig.16 where λ_{ne} and the density at the separatrix n_{es} are given as a function of time during the L- and H-phases of an NBI-heated discharge on ASDEX. Between ELMs both n_{es} and λ_{ne} remain at a constant value, although the line density increases by ~50%. Fig.17 depicts actual n_e profiles for three points during the H-phase. The virtual overlapping near the separatrix of these profiles is all the more remarkable when considering the traces are plotted with respect to a computed separatrix position which shifts by almost two cm over the time span. Thus the SOL appears to be "frozen-in" near values prevailing immediately after the L-H transition. Such behavior has also been observed on W7-AS with the lithium beam /2/, and from divertor measurements on JET (H_α, Langmuir probes) can also be inferred to take place in the ELM-free phase of high performance discharges /39/.

Turning to W7-AS, fig.18 gives 3D Li[2p] profiles over 20ms for the case where the main limiters constrict the plasma to a smaller bore, thereby increasing the radial extent of the SOL for more complete observation. Although the profiles are sampled at 5kHz, reproducibility is good. Profile fluctuations in the SOL are evident. Fig.19a gives the fluctuation amplitude normalized to the local value averaged over 20ms, illustrating these fluctuations are largely confined to the SOL and increase with greater distance from the LCFS. The spatial cross-correlation function between one SOL channel and all others (fig.19b) demonstrates the fluctuations are reasonably correlated over the whole of the SOL, i.e. by no means do they correspond to independent statistical fluctuations due to noise. Further, the correlation in the core is negative. These observations are consistent with fluctuations in n_{es} and λ_{ne}, which were also a regular feature of the ASDEX SOL.

4.3 Density Falloff Length Scalings in the SOL

Aside from monitoring fast events at the edge, systematic documentation of the parametric dependence of the core/SOL density profiles can be used to potentially learn something about

Dedicated density and power scans on W7-AS have enabled a (limited) systematic study of λ_{ne} via the Li-beam and Langmuir probes. From the Li-measurements one finds $\lambda_{ne} \sim$ $<n_e>_{vol}^{-0.43}$ $(P_{in} - P_{rad})^{0.25}$ /2, see also 45, 46/ for the combined set of scans (see fig. 23). Employing the simple formula for $D_\perp$ of above yields $D_\perp \sim$ $<n_e>_{vol}^{-1.1}$ $(P_{in} - P_{rad})^{0.85}$ /45/. Since the temperatures are high and limiters are in use, this Ansatz for deriving $D_\perp$ is more likely to be valid than for the case of a divertor. Although the given scaling for $D_\perp$ can be reformulated to include a very strong positive T_e dependence, the firm statement is that it is the density and not temperature which is governing the magnitude of transport. Core transport analysis on W7-AS also supports this view. Thus perpendicular transport on stellarators would seem to involve a strong and direct density component, for which there is little evidence on tokamaks in normal operating regimes.

5. Summary

High-energy neutral lithium beam probes to measure density profiles have attained the status of a standard diagnostic on W7-AS and ASDEX-Upgrade. Profile measurements on a sub-ms (≤ 0.2ms) basis and ≥ 0.5cm resolution are routine for cases where background light does not become too large. A system on DIII-D is dedicated to fluctuation measurements in the 100 kHz range. Both JET and TEXTOR are bringing Li-beam diagnostics into operation, using a gun of the IPP/Garching type, but either a CCD camera or photodiode array respectively as the detecting elements, instead of photomultipliers.

A reliable and easy-to-use neutral injector is available which can deliver 0.5 - 3 mA (equivalent) at energies of 20-70kV, while maintaining a beam FWHM of ~10mm at 2.3m downstream from the gun. However, operation at the higher currents places higher demands on the ß-eucryptite emitter quality, and is more difficult to achieve on a routine basis. The operating lifetime without a servicing break is adequate for present-day experiments running on a low duty cycle. Further developmental work on this or another type of ion gun is required if long-period measurements on next-generation steady-state machines are dictated. Of course, the present gun could be derated to lower currents to prolong lifetime, and synchronous detection techniques employed at the cost of reduced time resolution. On another front, ion guns based on an ECR plasma have the potential of higher-current DC operation. A system under initial development at the TU in Vienna, using a 2mm diameter accel-decel extraction

particle transport perpendicular to field lines. Fig. 20 presents ASDEX SOL profiles at four current values where $\overline{n_e}$ has been held constant at about 2.5×10^{13} cm^{-3} under conditions of pure Ohmic heating. With decreasing I_p a shoulder beyond R-R$_s$~2cm develops initially, followed by a decrease of n_{es} and a flattening of the profile near the separatrix, after which the entire SOL becomes still broader. The sharp break for R-R$_s$~5-6cm correlates with the last flux surface entering the divertor. Even in this simple current scan not only has I_p been varied, but also q_a and the input power. To evaluate the relative importance of these various factors and others on the profile shape, for example, requires a set of measurements spanning a broad range of independent parameter scans.

Fig. 21 summarizes the results of one such OH data set for ASDEX. A plot of λ_{ne} vs. T_s seems to suggest two different behavioral regimes. For $T_s > 40$eV the points scatter about ~1.9 cm and can be described by a scaling $\lambda_{ne} \sim q_a^{0.5} T_s^{0.25}$ /40/. For $T_s < 40$eV, the temperature dependence is reversed, where one finds $\lambda_{ne} \sim q_a^{0.8} T_s^{-0.5}$. Assuming that λ_{ne} reflects the SOL diffusion coefficient through the relationship $D_\perp \sim v_{||} \lambda_{ne}^2/L_c$ (where $v_{||}$ is parallel streaming velocity and L_c the midplane to divertor/limiter connection length), these parametric relationships are not inconsistent with the assumption of ExB-generated turbulent SOL transport where either the sheath resistance (high T_s regime) or plasma resistance (low T_s regime) in combination with bad field curvature are the driving forces /41/. Placing the expression for ($T_s > 40$eV) into the expression for $D_\perp$ leads immediately to $D_\perp \sim T_s$, or Bohm-like transport but without the field dependence /40/. However, single-fluid modelling of the situation using the fluid code B2 along with a simple divertor recycling model indicated that systematic changes in the Mach number as a function of density or power might well yield the same kind of observed behavior, without the need to invoke any change in transport /42/. Further discussion is beyond the scope of this paper.

Fig. 22 gives n_{es} and λ_{ne} during a ramp to the density limit on ASDEX-Upgrade for a high-q_a OH discharge /43/. The saturation of n_{es} (core density peaking) and increase in λ_{ne} with $\overline{n_e L}$ is reminiscent of the high-q_a, low-temperature-region SOL behavior of ASDEX on the way to a MARFE /44/. However, corroborative edge temperatures to permit a more detailed comparison with ASDEX are not available for this shot.

aperture, has produced a 12kV/1.2mA Li$^+$ beam, 70% of which could be detected within the 12mm diameter entrance orifice of a Faraday cup placed at a distance of 1.5m /47/.

The sodium- filled neutralizer exhibits a very low leak rate in the pulsed mode. Accepting higher overall losses, it can be modified in a fairly straightforward fashion for DC operation.

Experiments on W7-AS have shown that increasing the beam energy from 20 to 66keV does not lead to a dramatic increase in beam penetration. However, experience indicates it also does not significantly affect the spatial resolution of the diagnostic as one might expect when considering the 27ns lifetime of the Li(2p) level and corresponding beam velocities. On the positive side, for the IPP ion gun design, higher beam energies are synonymous with higher beam currents, which promote enhanced time resolution for a given signal-to-noise ratio for all applications of the Li-beam diagnostic. Moreover, requirements concerning the accuracy of $T_e(r)$ profiles used in carrying out density reconstruction are relaxed at larger beam velocities. On the CHS device, successful $n_e(z)$ measurements along the axis of an 8 kV Li^0 beam have been reported for $\overline{n_e z} \leq 2 \times 10^{13}$ cm^{-2} /24, 48/ - only a factor of two less than the $\overline{n_e z} \leq 4 \times 10^{14}$ cm^{-2} limit on W7-AS for $E_b \sim 30\text{-}66$keV.

The reconstruction algorithm for deriving absolute density profiles from the relative Li[2p] profile has been shown to function well over a wide range of plasma conditions and beam energies. It delivers values in good agreement with other diagnostics, attesting that the cross section database involving both electrons and ions is accurate and that the algorithm itself is in order. It has been shown that the end result depends only very weakly on the absolute values of $T_e(r)$ and $Z_{eff}(r)$, and so with generic estimates of both the method attains a stand-alone status. Density measurements along the beam line are possible for $\overline{n_e z} \leq 4 \times 10^{14}$ cm^{-2}. On W7-AS, where the beam traverses the plasma in a region of compressed flux surfaces, densities over the range from less than 10^{12} up to 10^{14} cm^{-3} are accessible, including the complete density gradient region of the core.

The feasibility of lithium-beam-activated CXRS has been demonstrated on TEXTOR in the proof-of-principle sense /49/. Systems to this same end are installed (or will be installed) on W7-AS (ASDEX-Upgrade). Should the beam intensity and impurity densities be adequate to attain a reasonable time resolution, this would represent an important parasitic application in

addition to the density determination, since the method is inherently non-perturbing and would represent a very local measurement due to the small beam diameter.

Proof-of-principle measurements of the neutral gas pressure outside the plasma column, in the Li-beam injection port of the torus, in the 10^{-6}-10^{-5} mbar range have been performed on W7-AS /1/. This is a lower pressure range than can normally be accommodated by the usual in-vessel ionization gauges. It is of relevance for regions far from strong plasma-wall interaction, and for investigations where main-chamber recycling is to be minimized, as for instance in the case of high performance H-modes. As the application requires almost no diagnostic preparation, it can be run in an entirely parasitic fashion with only the necessity to calibrate the system occasionally.

Figure Captions

Fig.1 The original version of the ASDEX gun, constructed in 1982 for operation up to 100kV. For the improved version of the gun, for which beam characteristics are reported here, the smaller tube has a inner diameter of 40mm instead of 30mm, and is spaced 35mm from the larger tube instead of 85mm.

Fig.2 Layout of the neutralizer.

Fig.3 (top) Neutralization efficiency of Li^+ on Na^o, and (bottom) equivalent neutral beam current vs. beam voltage. The fit functions over the voltage range are indicated. Note, the neutral beam current cannot be extrapolated beyond the curve, as I_b actually increases faster than the fit at low E_b and then begins to roll over at the highest energies. The extracted ion current from the emitter varies as $\sim V_{ext}^{1.5}$. The input powers are roughly: P_{tube} ~62 W (0.97A/65VAC), $P_{reservoir}$ ~17 W (0.84A/20VAC), and $P_{emitter}$ ~214 W (31.5A/6.8VAC).

Fig.4 Experimental setup on W7-AS. The z=0 reference point along the beam is indicated. The CXRS optics and neutral density measurement are briefly described in /33/.

Fig.5 (top) W7-AS experimental Li[2p] profile along with the background light. (bottom) Deconvolved density profile. The shaded band gives an estimate of the absolute error arising from statistical fluctuations in the background and lithium signals, and the relative calibration error in each of the channels.

Fig. 6 (top) Li[2p] profiles for V_b=20, 30, 48 and 66kV. #26404, #26405, #26408, #26410, respectively. (bottom) $n_e(z)$ profiles along the beam axis, reconstructed from the above Li[2p] traces. $\iota \sim 0.53$, $B_t = 2.53T$, $\overline{n_eL} \sim 1.9 \times 10^{19}$ m^{-2}, P_{in}~0.4MW.

Fig.7 (top) Li[2p] profiles for core line densities of $\overline{n_eL}$ ~1, 2, 3.3 and 4.3×10^{19} m^{-2}, (bottom) $n_e(z)$ derived from the corresponding Li[2p] profiles. ι ~0.34, B_t=2.54T, P~0.4MW.

Fig.8 (top) Gas puff rate. (middle) $\overline{n_eL}$ vs. time. (bottom) Density profiles at the indicated time points. Profile peaking after reduction of the gas puff is evident. ι~0.34, B_t=2.53T, P~0.4MW.

Fig.9 Li (2s-2p) excitation rates via: (top) electrons, (middle) protons and (bottom) sum.

Fig.10 The influence of $T_e(z)$ on the outcome of the reconstruction process for the $n_e(z)$ profiles of fig. 7 corresponding to $\overline{n_eL}$ ~1.2 and 4.3 $\times 10^{19}$ m^{-2}. The solid lines give $n_e(z)$ using the correct temperature profile (the "high" T_e-profile belongs to the "low" n_e-profile and vice-versa). The dashed lines show the reconstructed $n_e(z)$ using the interchanged T_e-profiles.

Fig.11 Influence of Z_{eff} on deconvolved n_e-profiles. (top) Z_{eff} profiles. An average ion charge of 5 is assumed to arrive at the impurity ion concentration. (bottom) n_e-profiles for a 60keV beam using Z_{eff}=1, 2.5 and for a 30keV beam using Z_{eff}=2.5. n_e for 60keV changes about 10%, whereas there is an imperceptible change for 30keV (not shown). Note that the density profiles using Z_{eff}=2.5, which is more likely than Z_{eff}=1, are in close agreement for 30 and 60keV.

Fig.12 Comparison of $n_e(r)$ profiles derived from Langmuir probes, the Li-beam and Thomson scattering. The Thomson left-hand-side profiles have been mirrored to the outside. # 27159. $\overline{n_e L}$ ~ 2.4×10^{19} m^{-2}, ι ~ 0.335, B_t = 2.53T, P ~ 0.4MW

Fig.13 Comparison of $n_e(r)$ profiles from the Li-beam and reflectometer. The reflectometer trace for $R_{eff} > 0.13$m is taken from the Li-beam for the purpose of initialization.

Fig.14 ASDEX: (top) Li[2p] traces from five adjacent channels for three pellets out of a series. The pellet injection time is delineated by the increase in Li[2p] inside the main plasma. (bottom) 3-D plot over the same time slice for all ten ASDEX channels. n_e at the edge is low enough such that Li[2p] conveys a good qualitative picture of the $n_e(r, t)$ development.

Fig.15 ASDEX: (top) 3-D plot of Li[2p] covering a span of 12ms during which two ELMs occur. (bottom) Decay in time of an ELM-associated density profile perturbation in the SOL. R-R_s is the distance from the separatrix.

Fig.16 ASDEX: Temporal behavior of λ_{ne} and n_{es} as well as other global plasma quantities during an ELMy H-mode phase. n_e is evaluated between ELMs. H^o->D$^+$, P_{in} = 2.8MW, B_t = 2.17 T, I_p = 315 kA.

Fig.17 n_e-profiles at various times during the H-mode period of fig.15. The SOL profiles between ELMs remain constant although $\overline{n_e}$ increases by 50% over this time.

Fig.18 W7-AS: 3D plot of Li[2p] illustrating the reproducibility of profiles at a 5kHz sampling rate and showing fluctuations in the SOL.

Fig.19 W7-AS: (top) Li[2p] fluctuation amplitude normalized to the local averaged value. (bottom) Cross-correlation between channel six (z~13.25cm) and all other channels.

Fig.20 ASDEX: SOL density profiles for an I_p scan. $\overline{n_e}$ ~ 2.5×10^{13} cm^{-3}, B_t = 2.2T, q_a ~ 2.6, 4.35, 5.5, 7.34. P_{OH} ~ 0.37, 0.21, 0.13, 0.09 MW.

Fig.21 ASDEX: λ_{ne} vs. T_s, the electron temperature slightly inside the separatrix, for an OH scan covering $\overline{n_e}$ = $0.8\text{-}3.5 \times 10^{13}$ cm^{-3}, I_p=150 - 420kA, B_t =1.9-2.55 T, D$^+$.

Fig.22 ASDEX-Upgrade: n_{es} and λ_{ne} vs. $\overline{n_e L}$ for an OH discharge. I_p = 600kA, q_{95} = 5.

Fig.23 W7-AS: λ_{ne} in the SOL vs. the fit function for a density- and power-scan. $\overline{n_e}$ ~1.5×10^{19} m^{-3}, P_{in}-P_{RAD} ~ 0.13-0.62MW; P_{in}-P_{RAD} ~ 0.46MW, $\overline{n_e}$ ~1.5- 5.2×10^{19} m^{-3}.

References:

[1] K. McCormick, S. Fiedler, P.Platzer, J. Schweinzer, D. Wutte and S. Zoletnik, 21st EPS Conf. **18B** (Montpellier, 1994) 1268

[2] G. Kocsis, S. Zoletnik, S. Fiedler, P. Grigull, G. Heere, K. McCormick and J. Schweinzer, Proc. 22nd EPS Conf. **19c** (Bournemouth, 1995) III-269

[3] D.M. Thomas, Rev. Sci. Instrum. **66** (1995) 806

[4] A. Komori, et al., Nuclear Fusion **28** (1988) 1460

[5] K. Kadota, K. Tsuchida, Y. Kawasumi, and J.Fujita, Plasma Physics **20** (1978) 1011

[6] K. McCormick, H. Murmann and El Shaer, J. Nucl. Mater. **121** (1984) 48

[7] K. McCormick, et al., Rev. Sci. Instrum. **56** (1985) 1063

[8] P. Bogen and E. Hintz, 1986 *Physics of Plasma Wall Interaction in Controlled Fusion,* ed. D.E. Post and R. Behrisch (New York, Plenum Press)

[9] E. Hintz and B. Schweer, Plasma Physics and Controlled Fusion **37** (1995) A87

[10] J. Schweinzer, et al.Plasma Phys. Control. Fusion **34** (1992) 1173-1183

[11] Z.A.Pietryzk, P.Breger and D.Summers, Plasma Phys. and Contr. Fusion **35** (1993) 1725

[12] R. K. Janev et al. INDC(NDS)-**267** IAEA Nuclear Data Section, Vienna (1993)

[13] J. Schweinzer, D. Wutte, HP. Winter, J.Phys.B:At.Mol.Opt.Phys. **27** (1994) 137-153

[14] J. Schweinzer et al., Comp. Phys. Comm **88** (1995) 83

[15] J. Fujita and K. McCormick, 6th EPS Conf. (Moscow, 1973) 191

[16] K. McCormick, M. Kick and J. Olivain, 8th EPS (Prague, 1977) 140

[17] K. McCormick, F.X. Söldner, D. Eckhartt, F. Leuterer and H. Murmann, Phys. Rev. Letters **58** (1987) 491

[18] O. Heinz and R.T. Reaves, Rev. Sci. Instrum. **39** (1968) 1229

[19] K. McCormick and M. Kick, IPP Report III/85 (March, 1983)

[20] S. Fiedler, doctoral thesis , IPP-Report III/209 (October 1995)

[21] J.Schweinzer, S.Fiedler, O.Gehre, G.Haas, J.Neuhauser, D.Wutte and HP.Winter, 21st EPS Conf. (Montpellier, 1994)

[22] KFA-IPP-IB-04/94 Report, Workshop on Beta-Eucryptite Ion Sources (1994, Jülich)

[23] H. Iguchi, K. Kadota, K. Takagi, T. Shoji, M. Hosokawa, M. Fujiwara and K. Ikegami, Rev. Sci. Instrum. **56** (1985) 1056

[24] S.Sasaki, S.Takamura, M.Ueda, H.Iguchi and J.Fujita, Rev. Sci. Instrum. **64** (1993)1699

[25] X. Zhang, Z. Wang and L. Hu, Rev. Sci. Instrum. **65** (1994) 1231

[26] D. M. Thomas, W.P. West and K. McCormick, Rev. Sci. Instrum. **59** (1988) 1735

[27] A. Pospieszcyk et al., J. Nucl. Mater. **162-164** (1989) 574

[28] J.P. Blewett and E.J. Jones, Phys. Rev. **50** (1936) 464

[29] S.K. Allison and M. Kamegai, Rev. Sci. Instrum. **32** (1961) 1090

[30] F.M. Johnson, RCA Rev. **23** (1962) 427

[31] A. Septier and H. Leal, Nuc. Instrum. and Methods **29** (1964) 257

[32] R.K. Feeney, W.E. Sayle II and J.W. Hooper, Rev. Sci. Instrum. 47 (1976) 964

[33] W. Möller and K. Kamke, Nuc. Instrum.and Meth. **105** (1972) 173

[34] K. McCormick, IPP Report III/82 (March, 1983)

[35] P. Breger, JET Joint Undertaking, private communication (1995)

[36] P. Breger, R.W.T. König, C.F. Maggi, Z.A. Pietrzyk, D.D.R. Summers, H.P. Summers, and M.G. von Hellermann, 22nd EPS Conf. **19c** (Bournemouth, 1995) II-377

[37] G. Vlases et al., Nuclear Fusion **27** (1987) 351

[38] G.K. McCormick and Z.A. Pietrzyk, J. Nucl. Mater. **162-164** (1989) 264

[39] K. McCormick, J. Ehrenberg, A. Loarte, R. Monk, R. Simonini, J. Spence, M. Stamp, A.Taroni and G.Vlases, Proc. 22nd EPS **19c** (Bournemouth, 1995) I-313

[40] K. McCormick, G. Kyriakakis, J. Neuhauser, E. Kakoulidis, J. Schweinzer and N. Tsois, J. Nucl. Mater. **196-198** (1992) 264

[41] M Endler, L. Giannone, K. McCormick, H. Niedermeyer, A. Rudyi, G. Theimer and N. Tsois, J. of Nucl. Mater. **220-222** (1995) 293

[42] K.McCormick, et al., 20th EPS Conf. Lisbon **17C** (1993) II-587

[43] J. Schweinzer, S. Fiedler, O Gehre, G. Haas, J. Neuhauser, D. Wutte and HP. Winter, 22nd EPS Conf. **19c** (Bournemouth, 1995) III-253

[44] K.McCormick, J.Schweinzer, Z.A.Pietrzyk, 19th EPS Conf. Innsbruck **16C** (1992) 763

[45] F. Feng et al., 22nd EPS Conf. **19c** (Bournemouth, 1995) IV-327

[46] P. Grigull, et al., 10th Int. Stellarator Conf. (Madrid, 1995)

[47] D. Wutte, Inst. für Allgemeine Physik, TU-Wien, private communication (1996)

[48] M. Ueda, H. Iguchi, S. Sasaki and J. Fujita, J. Nucl. Mater. **196-198** (1992) 923

[49] R.P. Schorn, E. Hintz, D. Rusbüldt, F. Aumayr, M. Schneider, E. Unterreiter and H.P. Winter, Appl. Phys. B **52** (1991) 71

CERAMIC INSULATOR

ARMCO IRON

MUMETAL SHIELD

Bellows

SF$_6$ PRESSURE VESSEL

2-TUBE LENS

EMITTER

EXTRACTOR

HV Cable

ELECTROSTATIC BARRIER
APERTURE

X-Y DEFLECTION
PLATES

NEUTRALIZER

Turbo
Pump

Turbo
Pump

10 cm

IPP3- MCC 275-83

Fig. 1: Li-Beam Gun with original 1982 dimensions
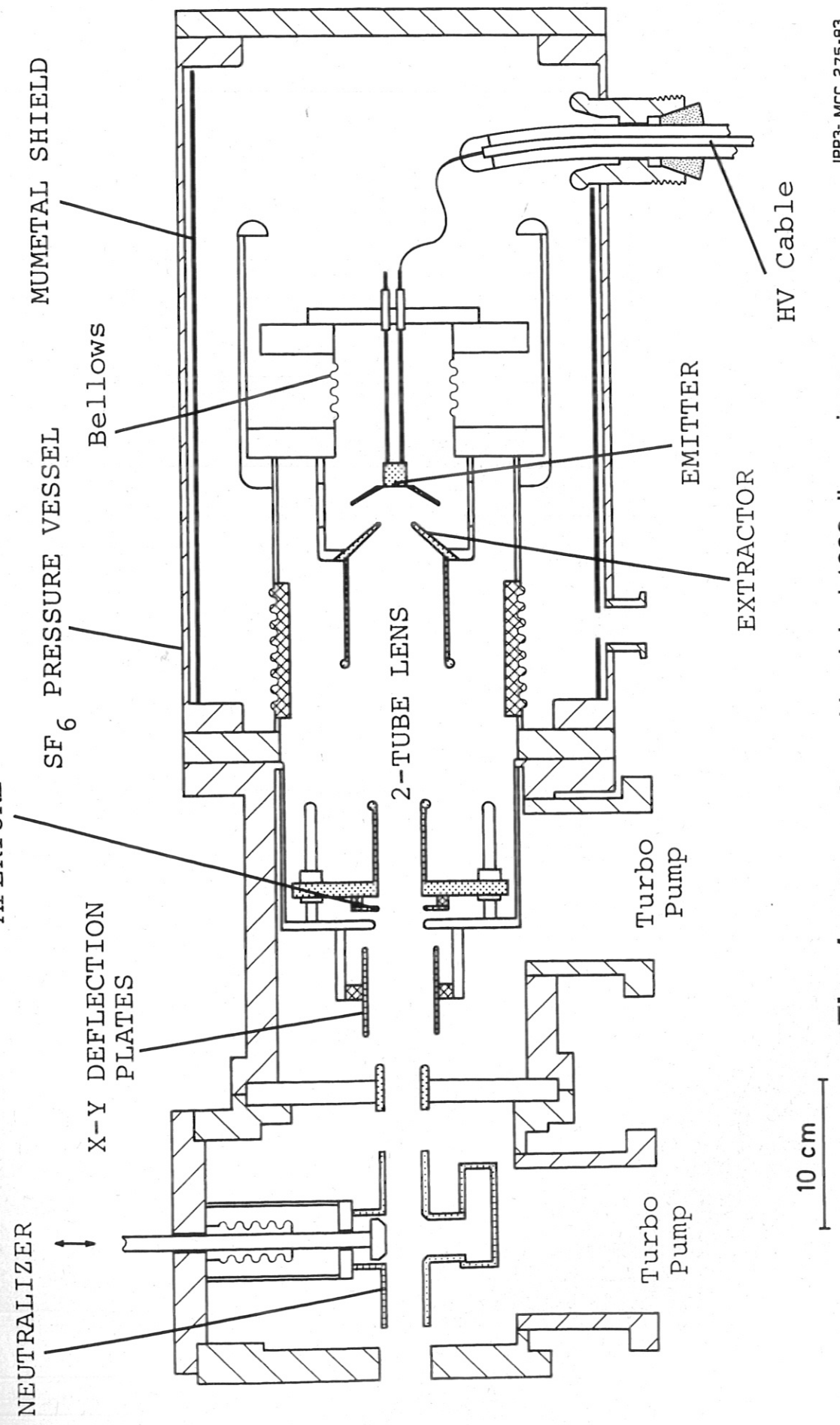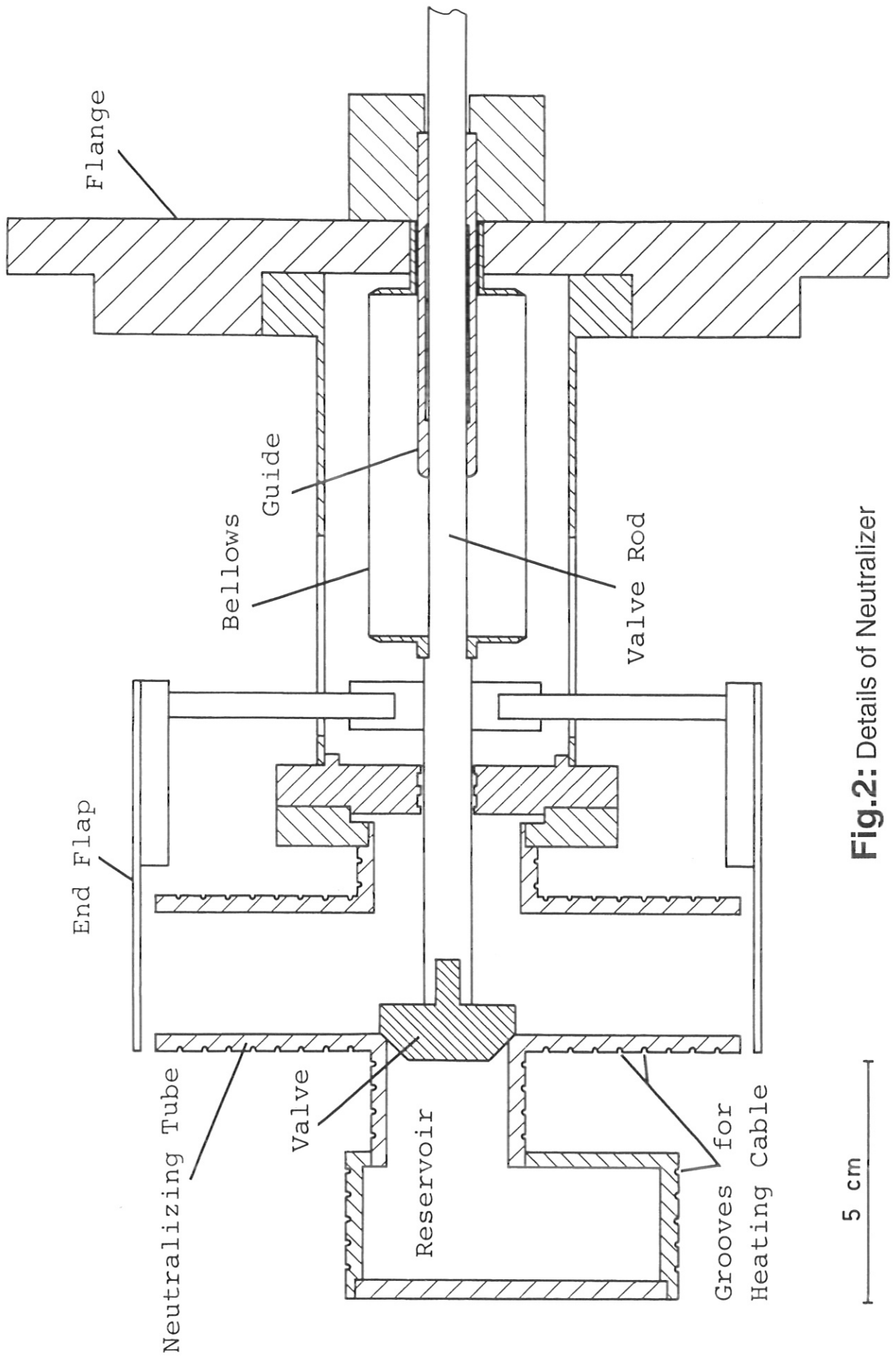
Fig.2: Details of Neutralizer

Flange

Bellows

Guide

Valve Rod

End Flap

Neutralizing Tube

Valve

Reservoir

Grooves for
Heating Cable

5 cm

IPP3- MCC 714-82

Top chart — Neutralization Efficiency [%]

$$Y = M0*e^{M1*X}$$

M0	106.64
M1	-0.0064615
R	0.9868

reservoir temp. ~ 235-240 °C
tube temp. ~ 310 °C

[keV]

Bottom chart — I_{beam} [mA equiv.]

$$0.0096 E_b^{1.36}$$

E_{beam} [keV]
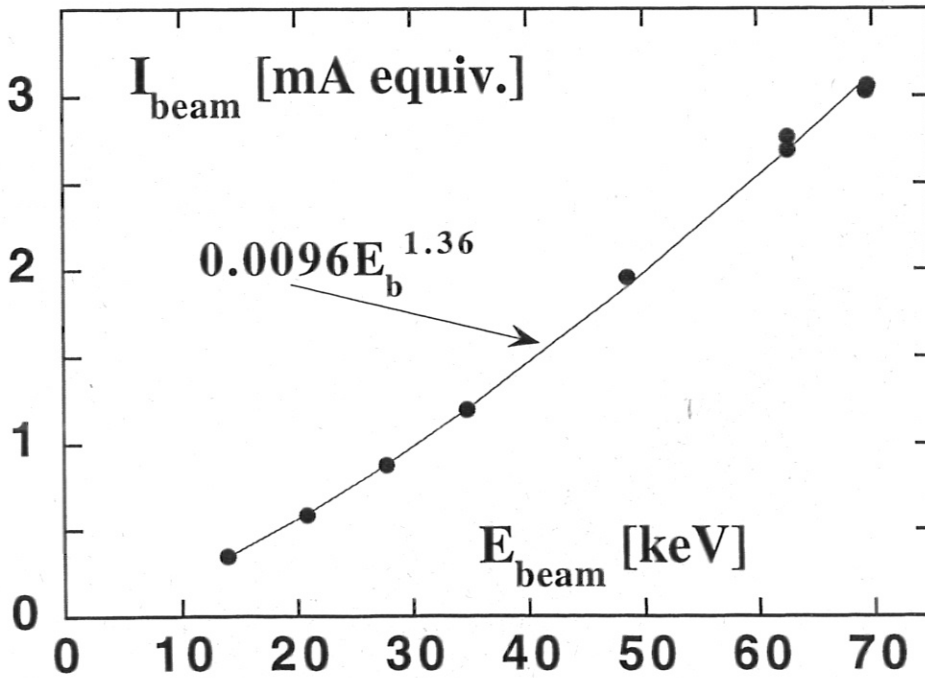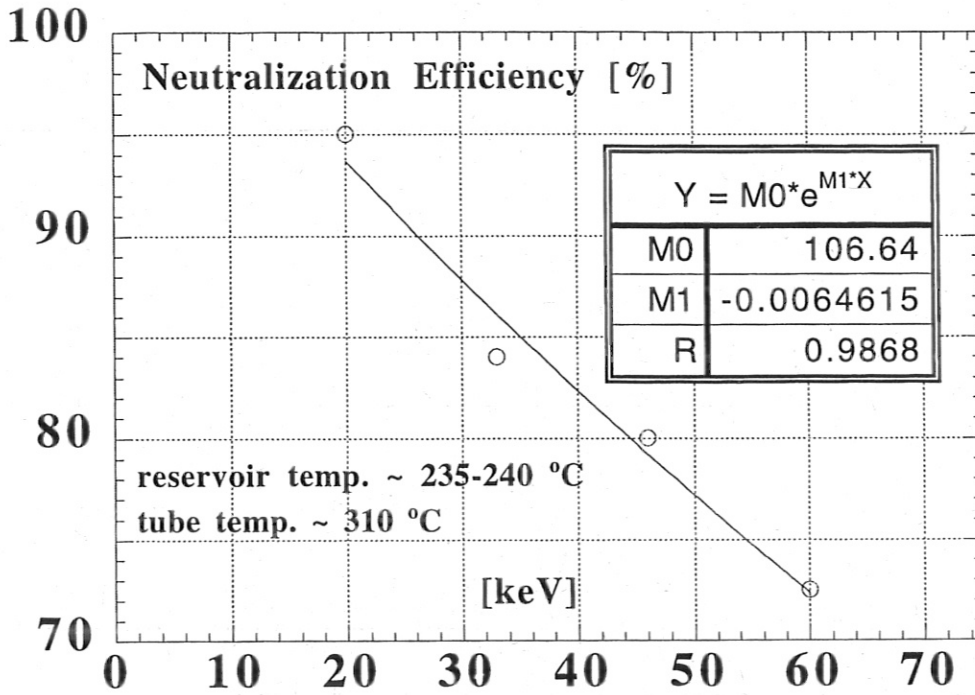
Fig.3: Neutralization efficiency (top), and equivalent neutral beam current (bottom) vs. beam voltage. The fit functions over the voltage range are indicated. P_{tube} ~ 62 W, $P_{reservoir}$ ~ 17 W. $P_{emitter}$ ~ 214 W.

W7 AS Li - Beam Diagnostic

module 2, -18 degree

beam coordinate z

Li - beam
20 - 66 keV
0.5 - 3.0 mA

detection of
Li(2p) light for
determination of
neutral density

Hα
detection

14 channel detection of impurity
line radiation for determination
of impurity density profiles

28 channel detection of Li(2p) light
for determination of electron
density profiles with high
spatial ($\Delta r \approx 0.5$cm) and
temporal ($\Delta t \approx 0.2$ms) resolution
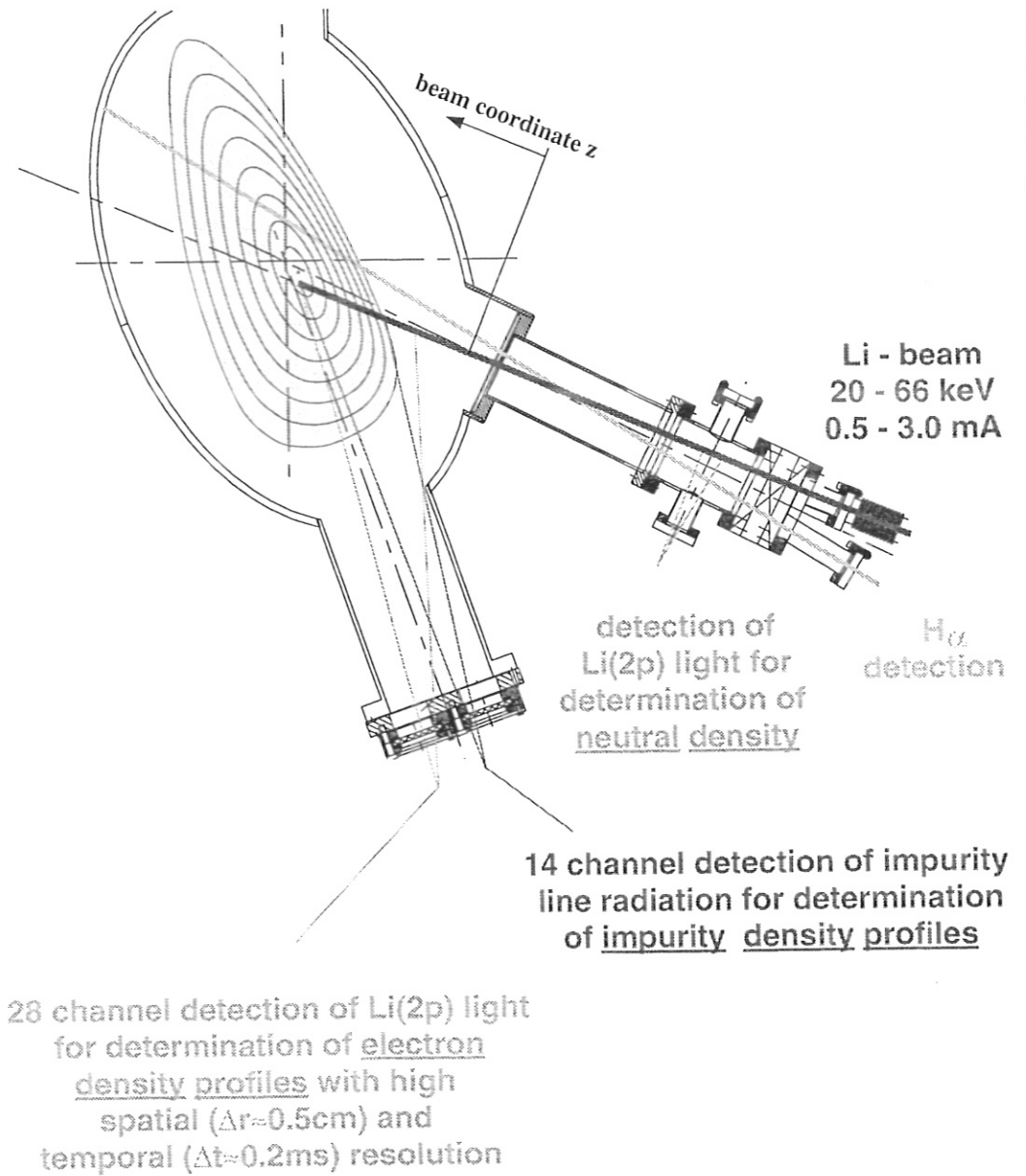
Fig. 4: Layout of Li-Beam on W7-AS
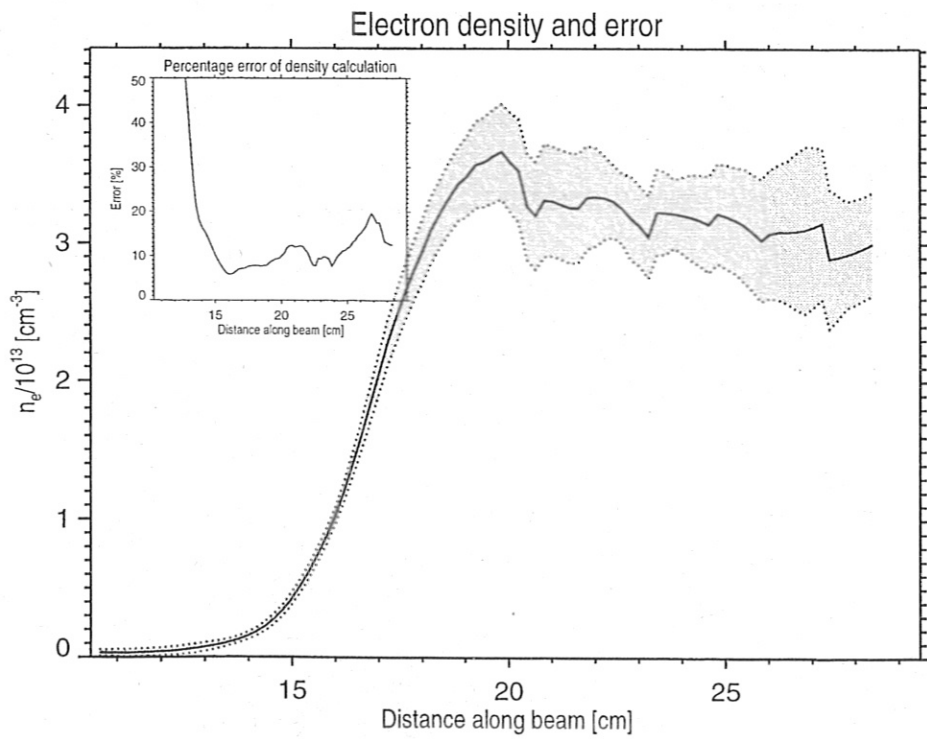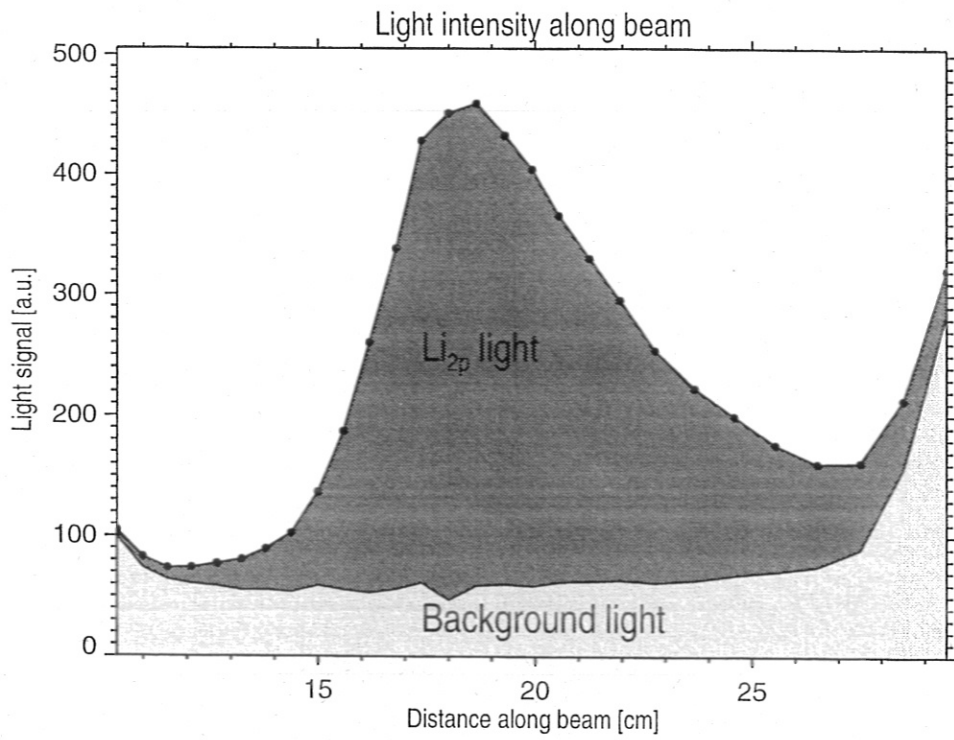
Fig.5: Li(2p) profile and background light (top), $n_e(z)$ profile with error bands.
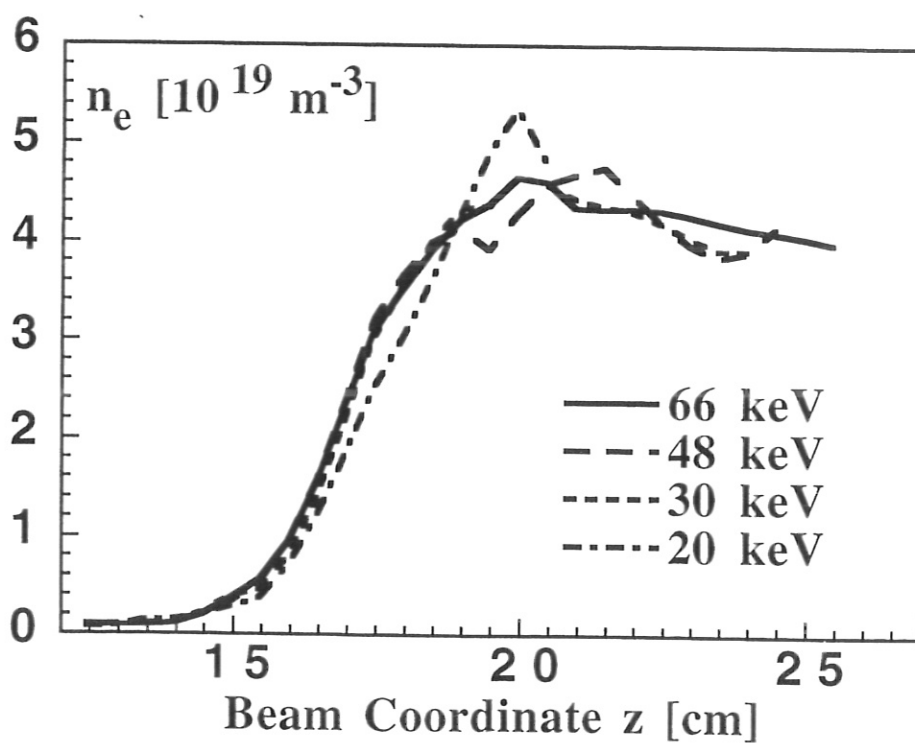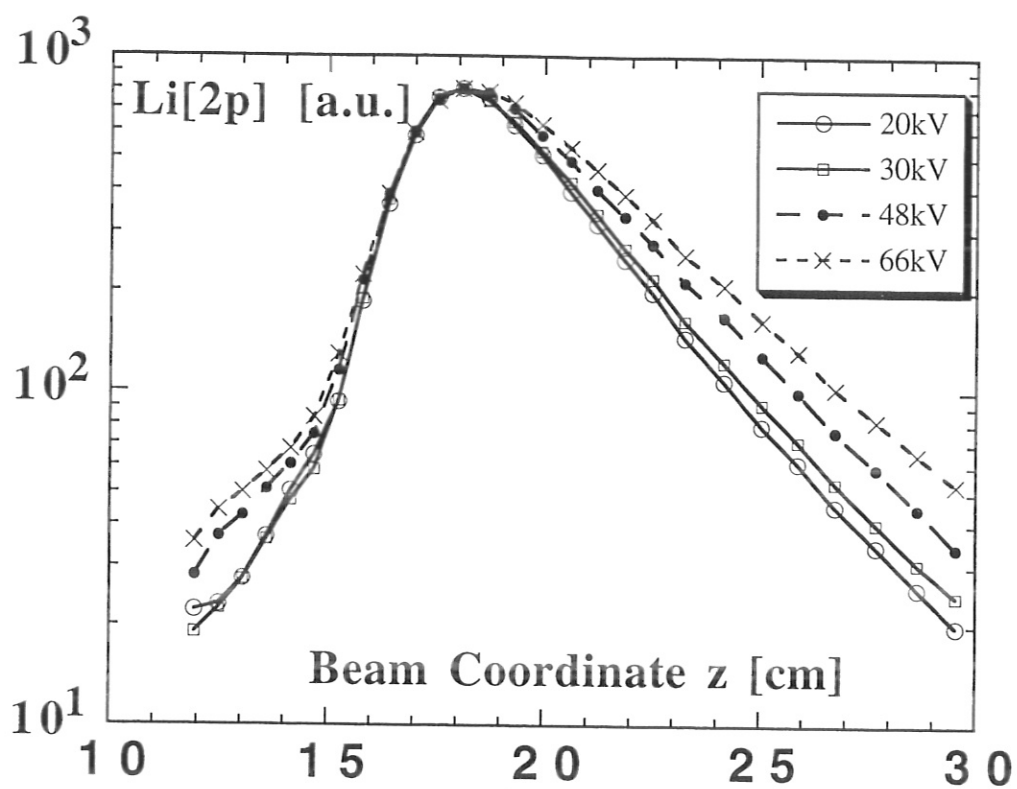
Fig. 6: Li(2p) profiles (top), corresponding density profiles (bottom)
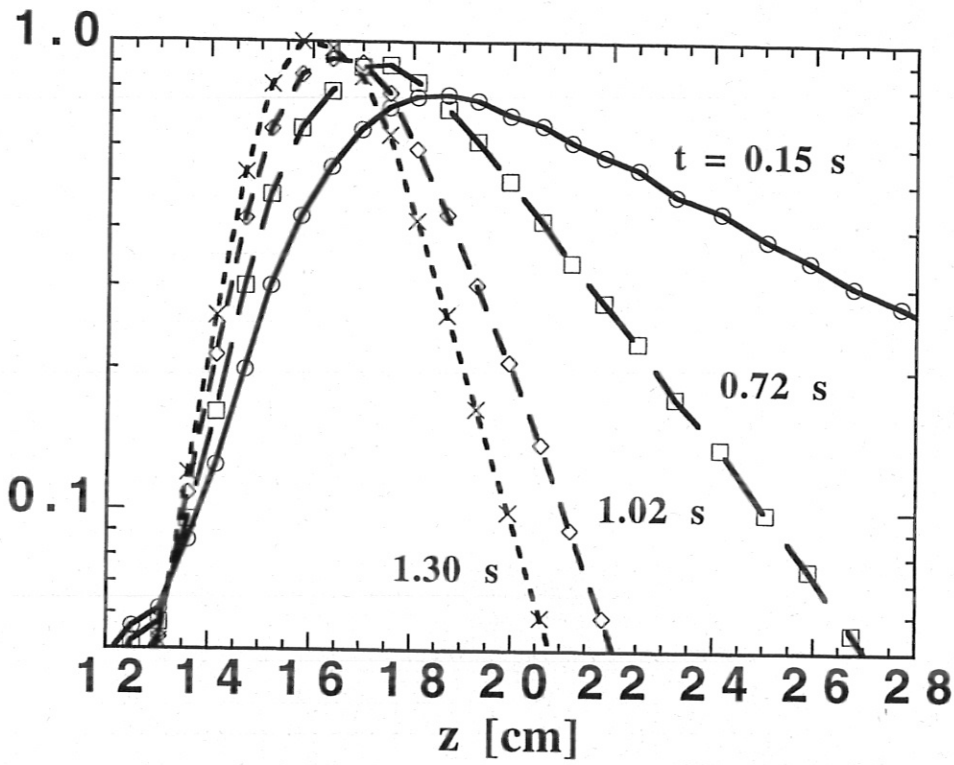
26439
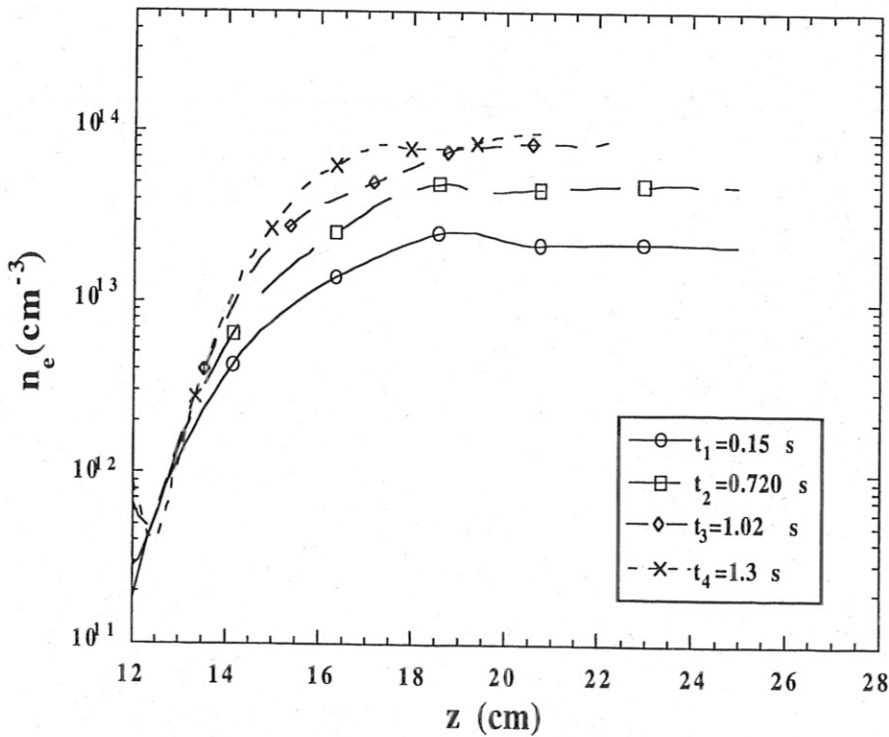
Fig. 7: Li(2p) profiles (top), corresponding density profiles (bottom)
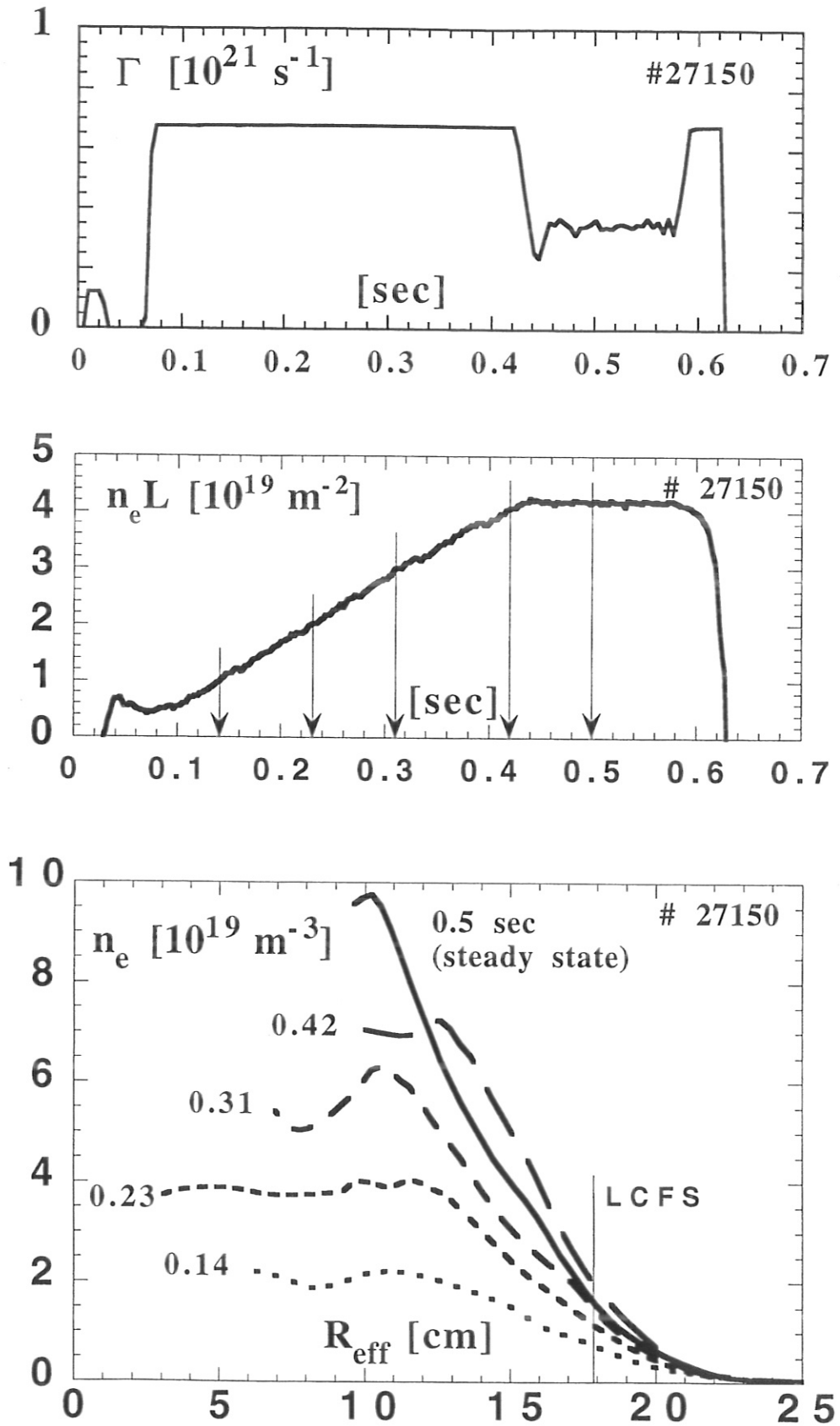
Fig. 8: Gas puff rate (top), $\overline{n_e L}$ vs. time (middle); $n_e(r)$ profiles during ramp and steady-state (bottom)
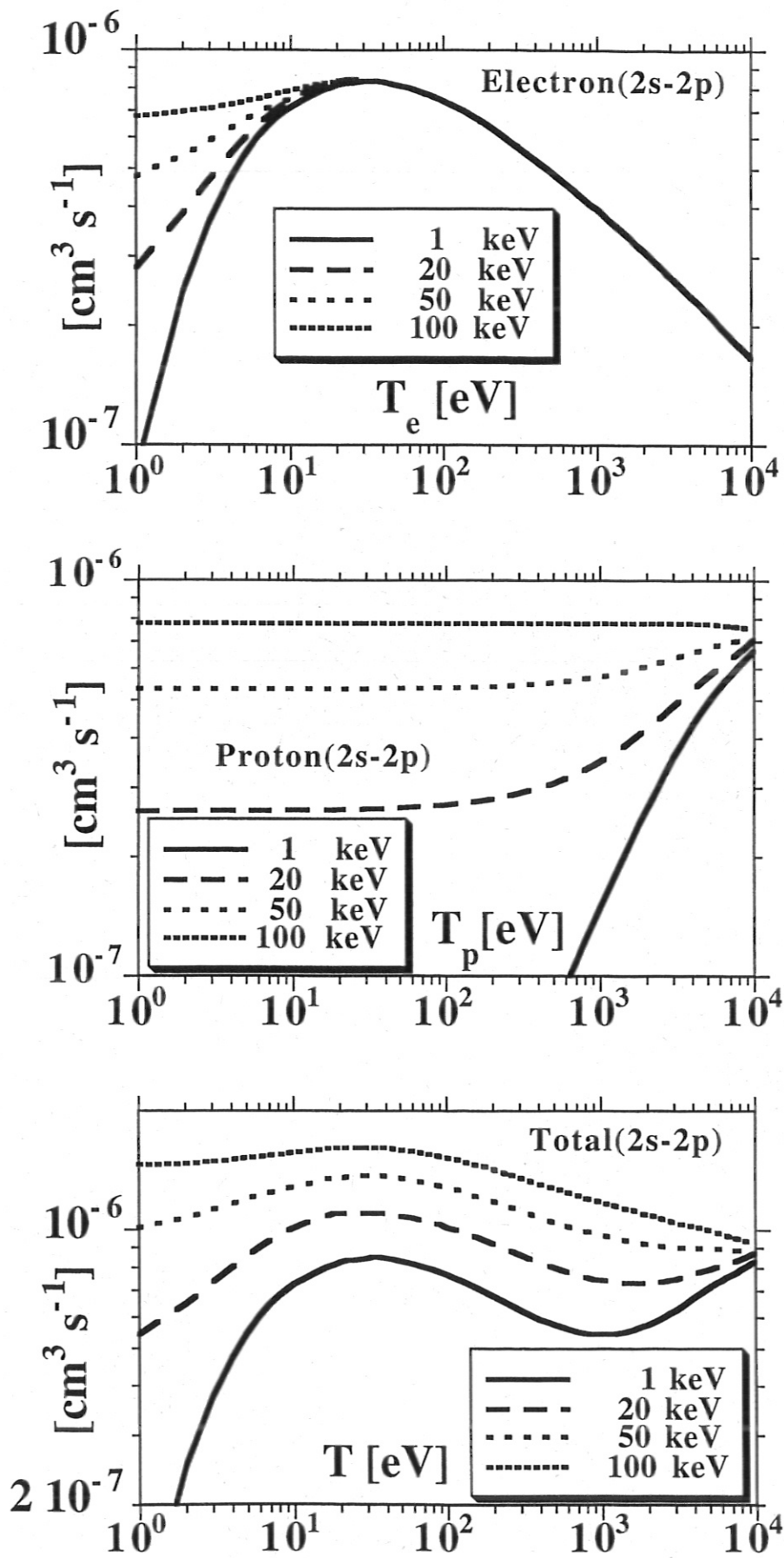
Fig. 9: Li(2s-2p) excitation rates- electrons (top), protons (middle), total (bottom)
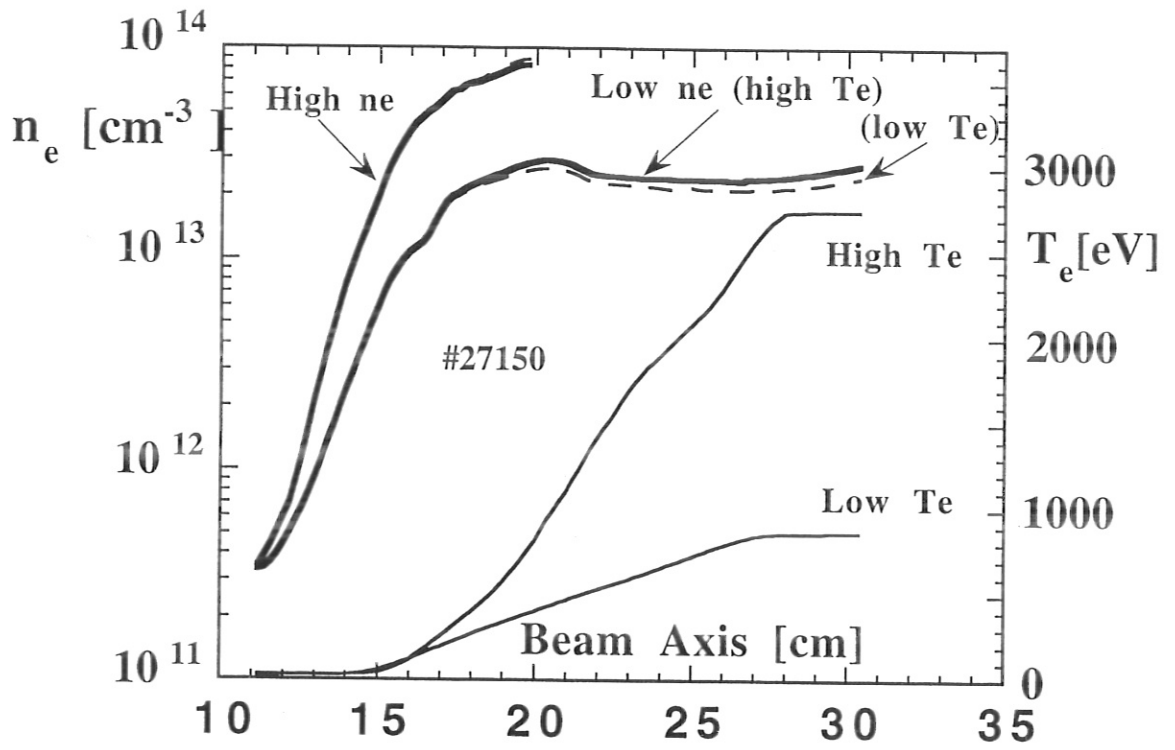
Fig. 10: Sensitivity of $n_e(r)$ deconvolution to the $T_e(r)$ profile.
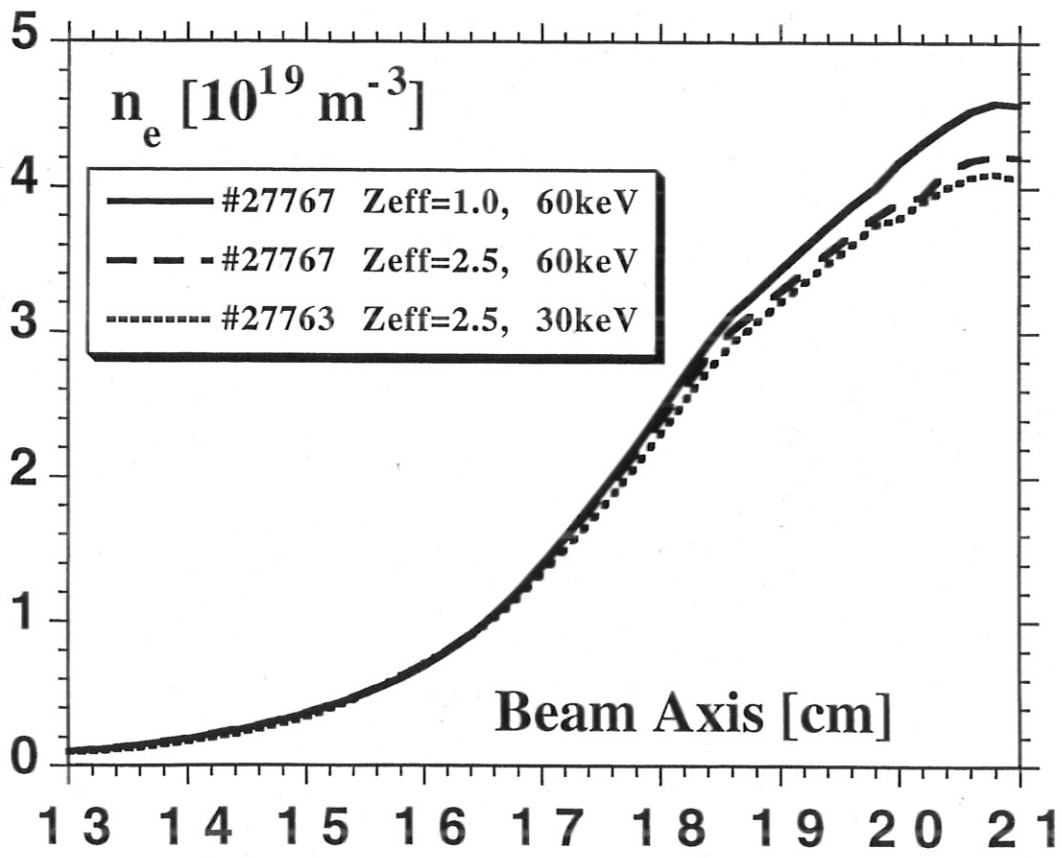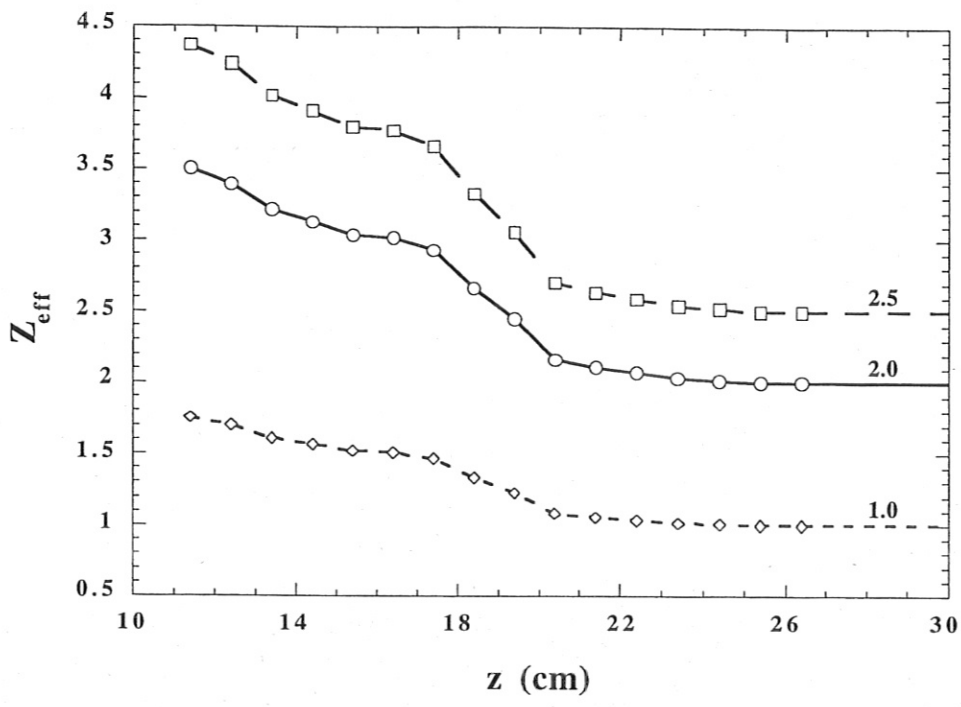
Fig. 11: Z_{eff} profile used for deconvolution (top), deconvolved $n_e(r)$ (bottom)
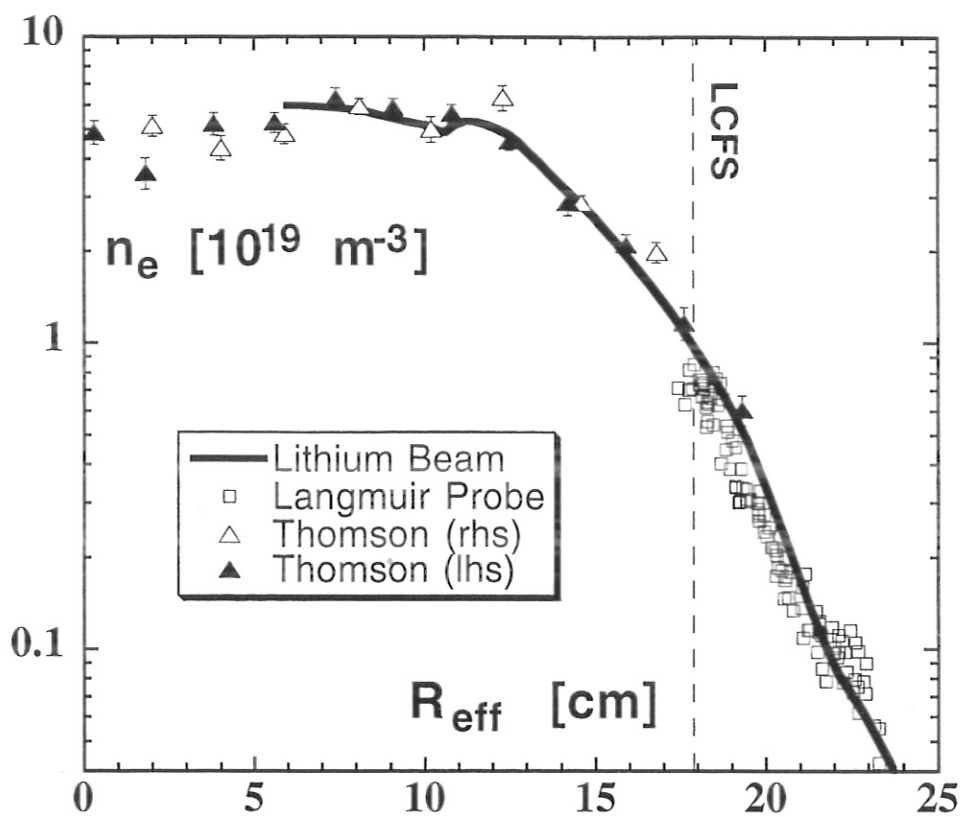
Fig. 12: Comparison of $n_e(r)$ profiles from Thomson scattering, the Li-beam, and Langmuir probe. #27159
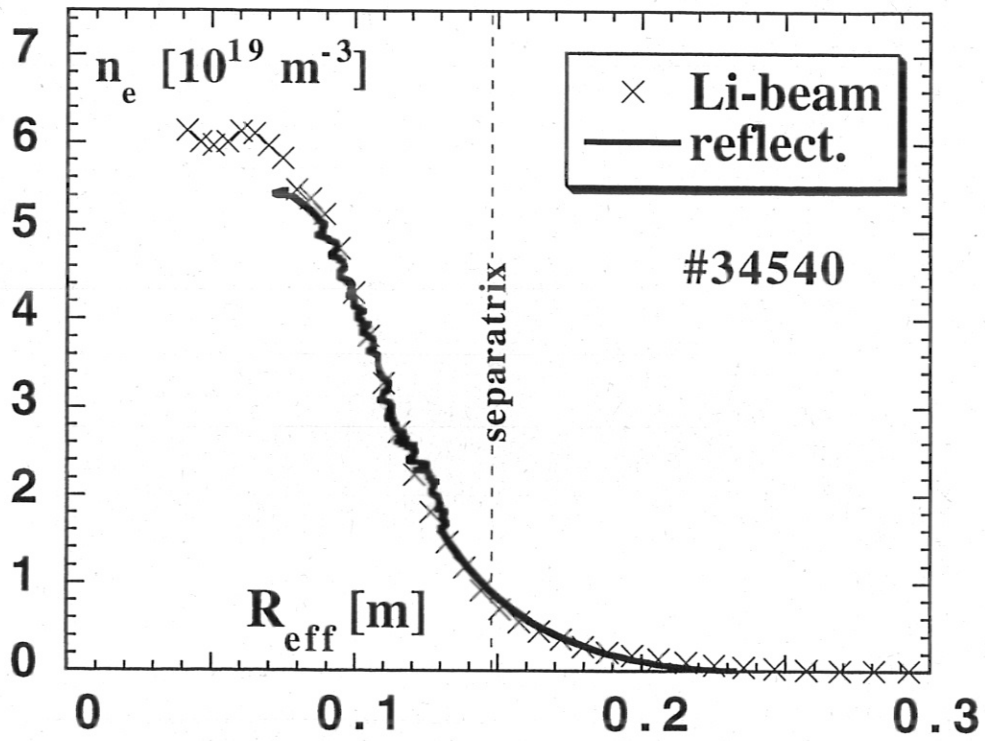
Fig. 13: Comparison of $n_e(r)$ profiles from the Li-beam and reflectometer.
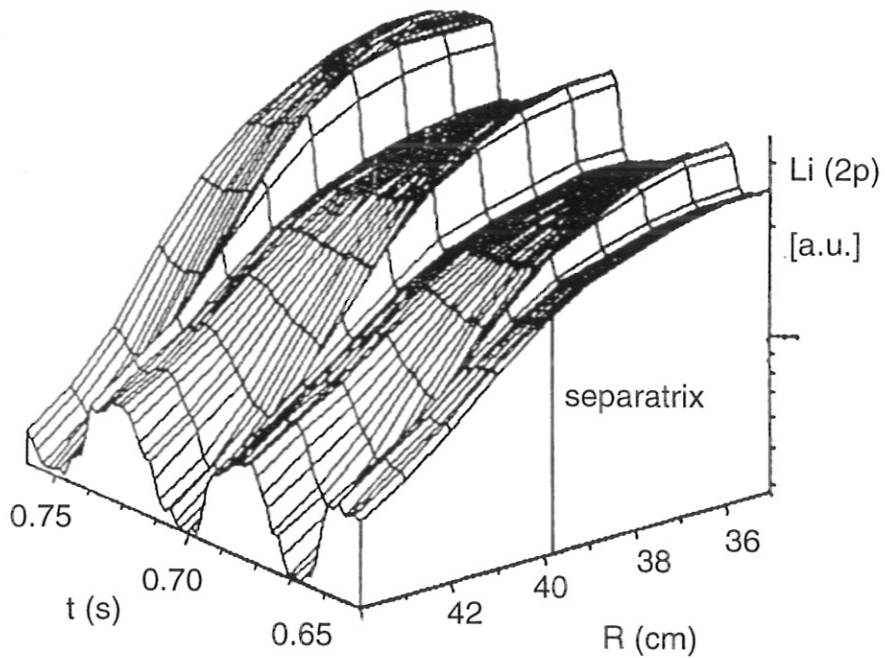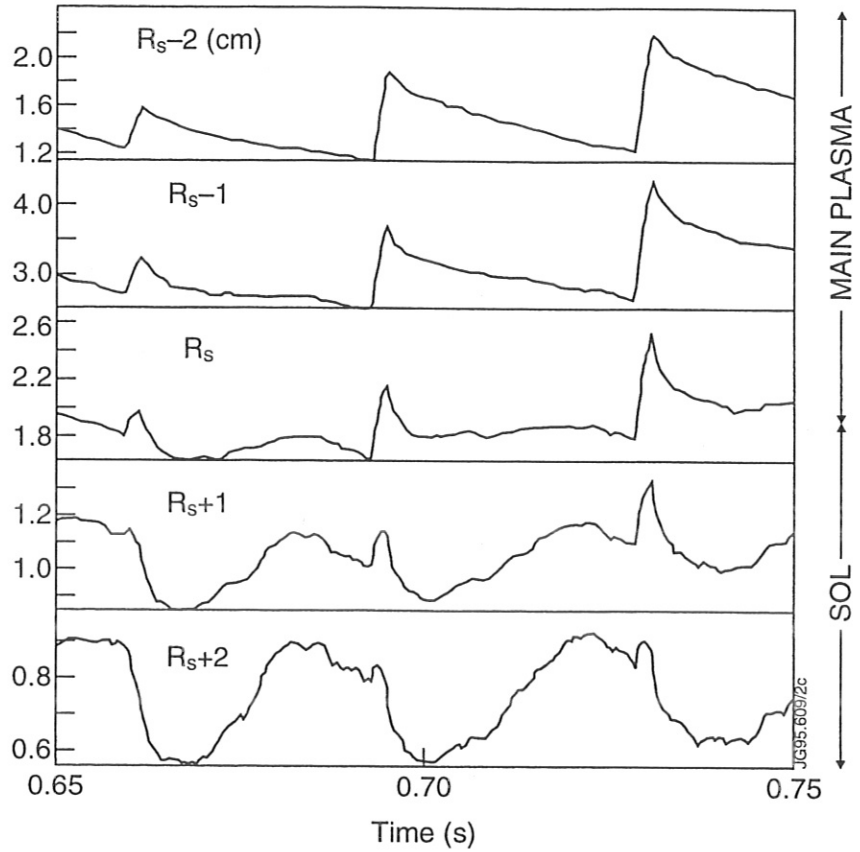
Fig. 14: Li(2p) time traces at five radial points centered about the separatrix (top), corresponding 3-D picture of the Li(2p) intensity (bottom). Three pellets are injected during the 100 ms time span.

9630

Li [2p-2s] [a.u.]

Separatrix

[sec]

1.220   1.215   1.21044   42   40   38   36

R-165 [cm]

IPP 3 MCC 564-88

separatrix

#9633

10^{13}

n_e [cm^{-3}]

ELM

1.2107 s

1.2111 s

1.2114 s

1.2120 s

10^{12}

H-mode

1.2133 s

-4   -2   0   2   4   6

R - R$_S$ [cm]
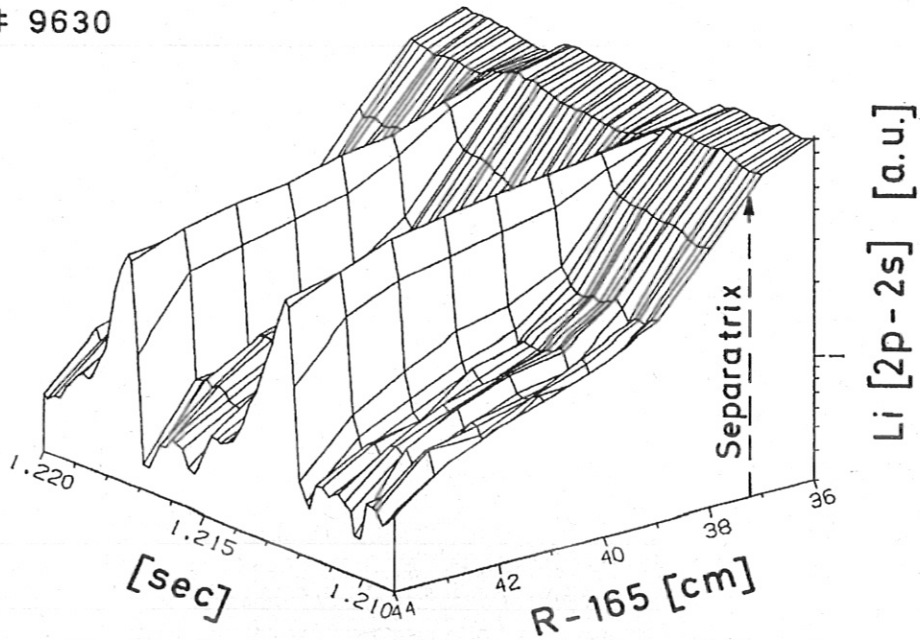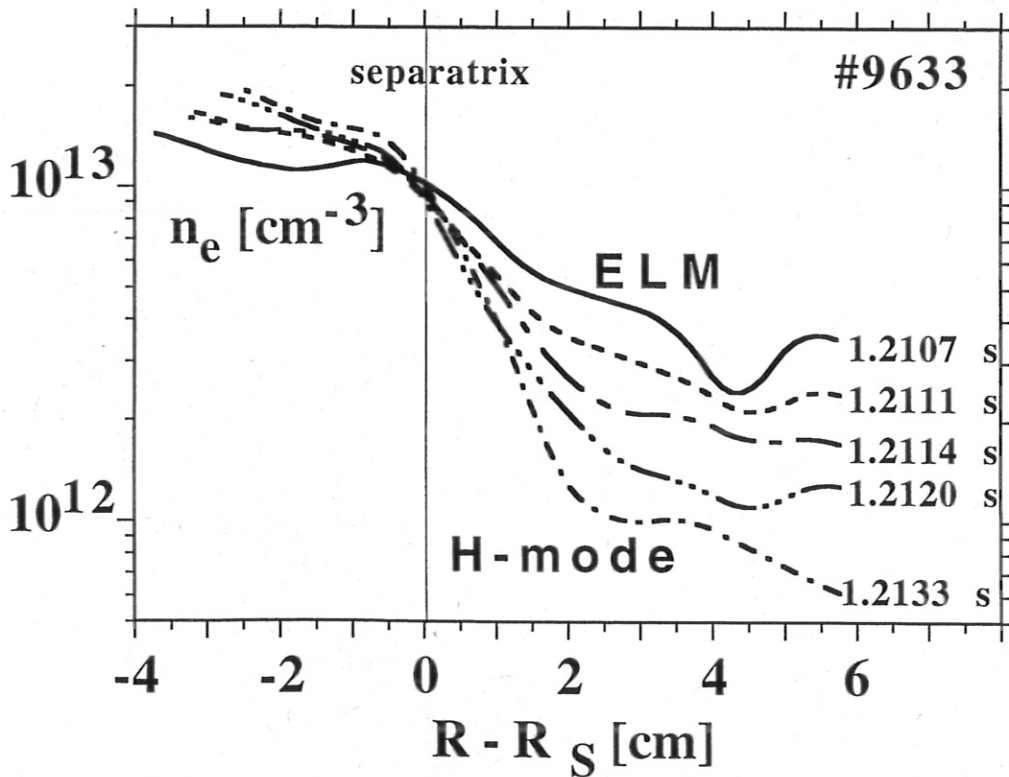
Fig. 15: 3-D plot of the Li(2p) intensity over a time encompassing two ELMs (top), n_e(R-R$_S$) profiles during the decay period of an ELM (bottom). **ASDEX**
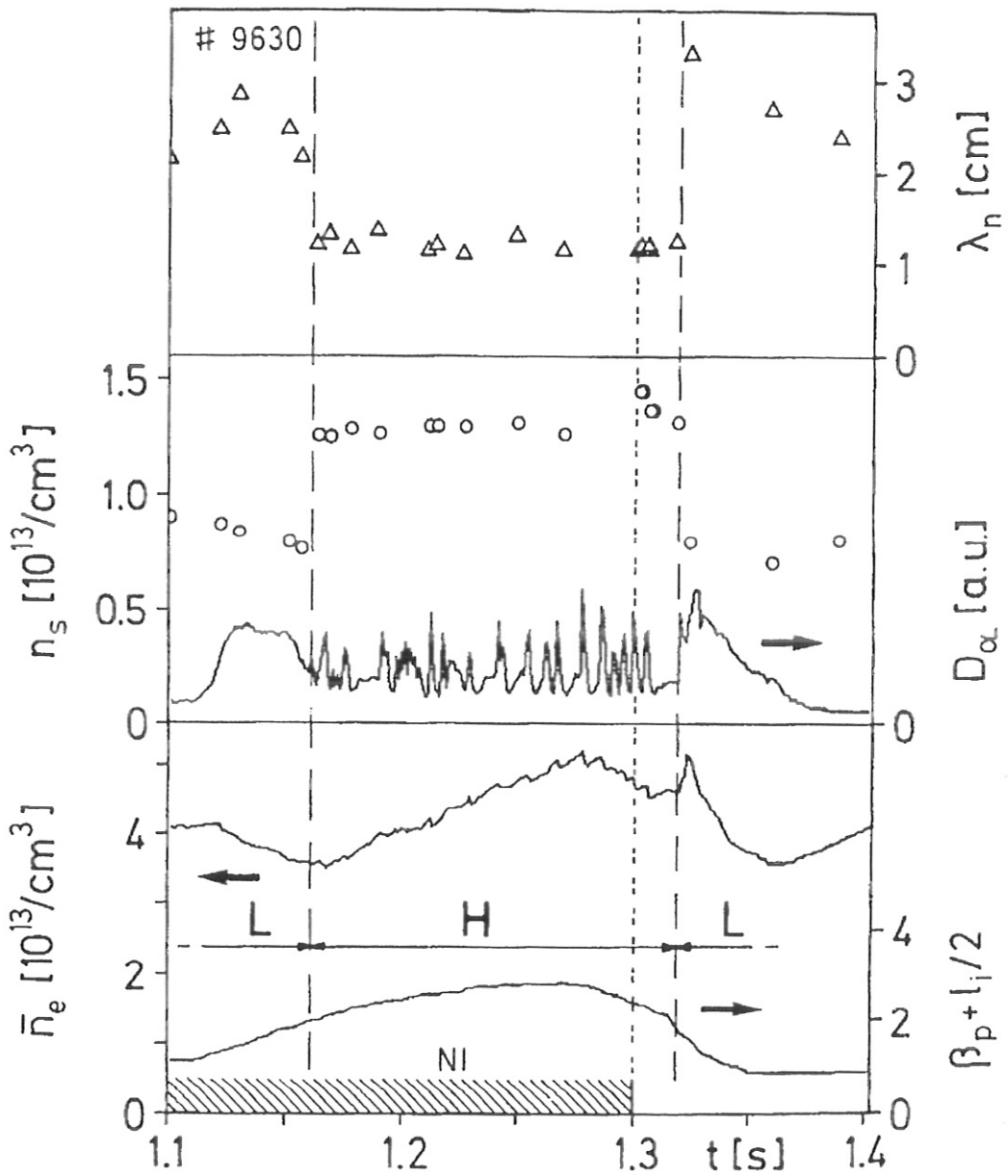
Fig. 16: Time traces of λ_{ne}, n_{es}, D_α, $\overline{n_e}$, $\beta_p+l_i/2$ during and after an NI-phase on **ASDEX**.
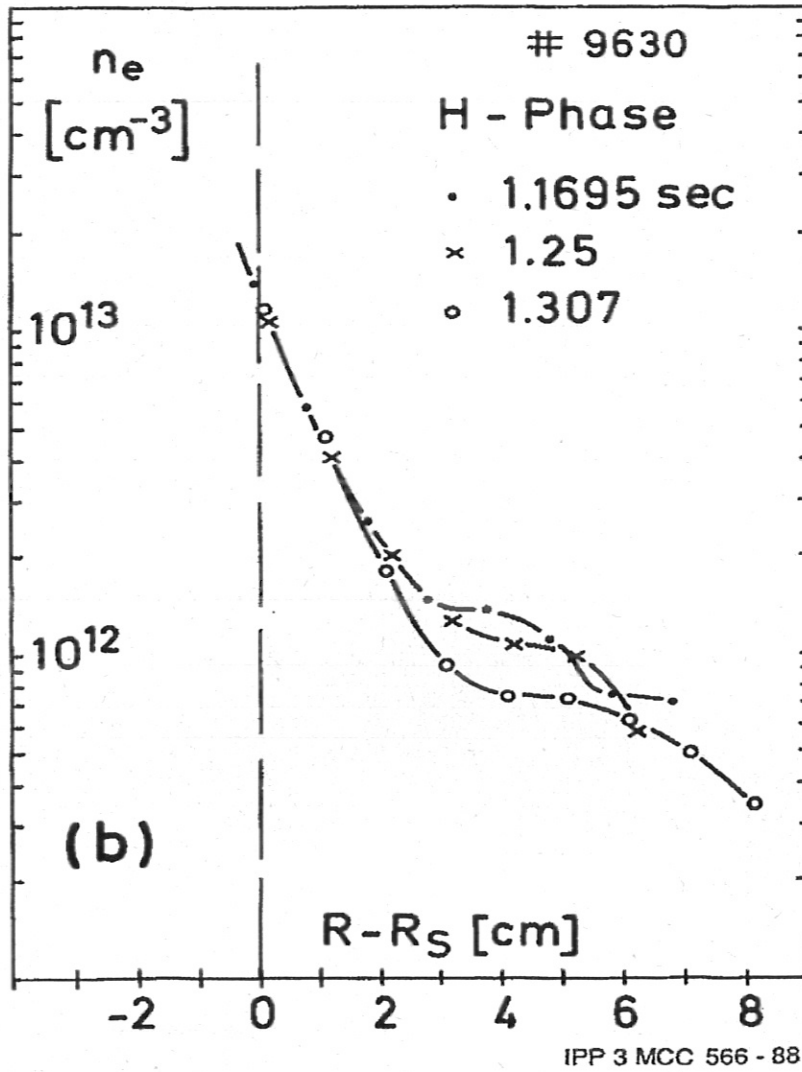
Fig. 17: $n_e(R-R_S)$ profiles at various times during the quiescent H-mode phase.
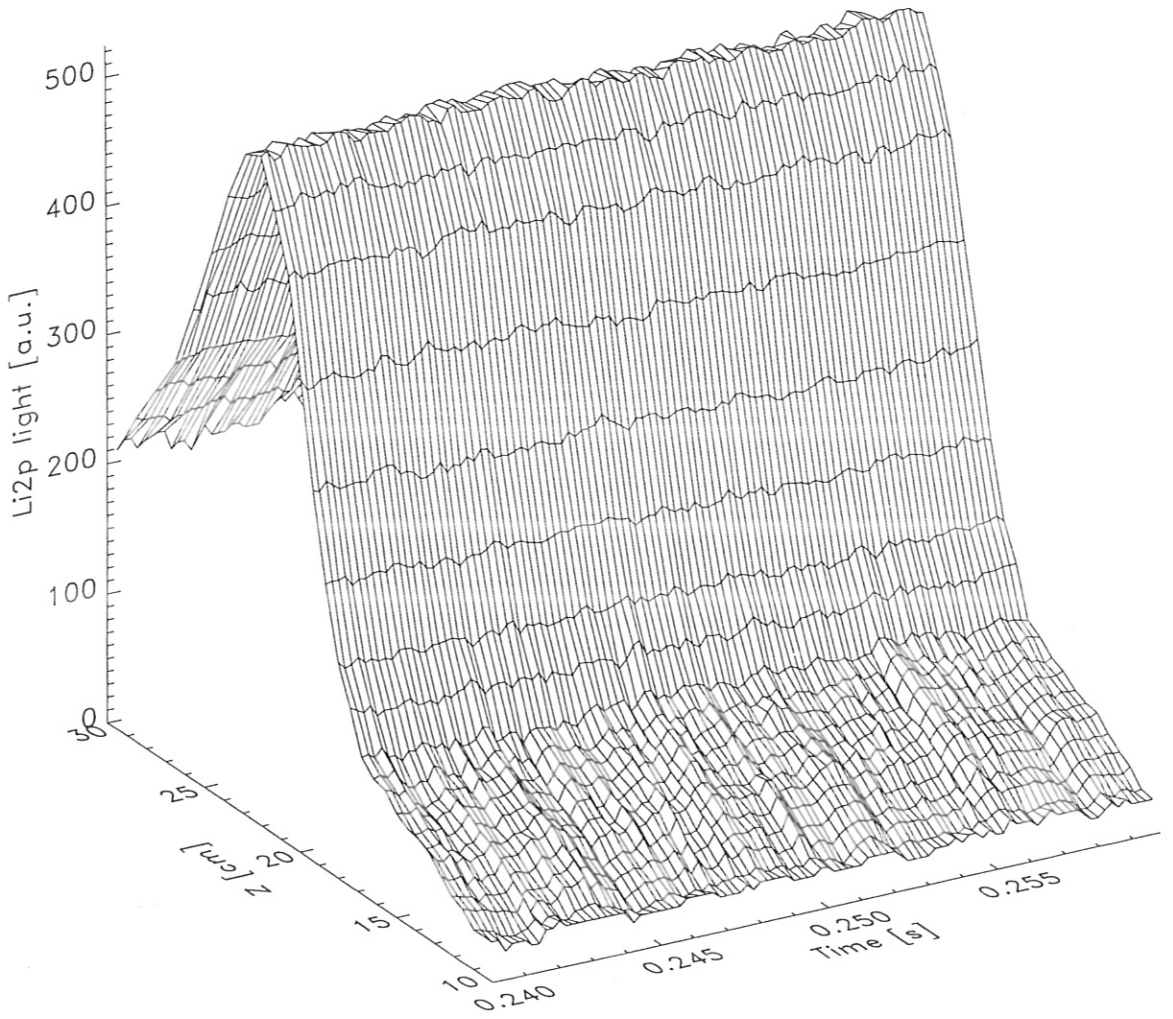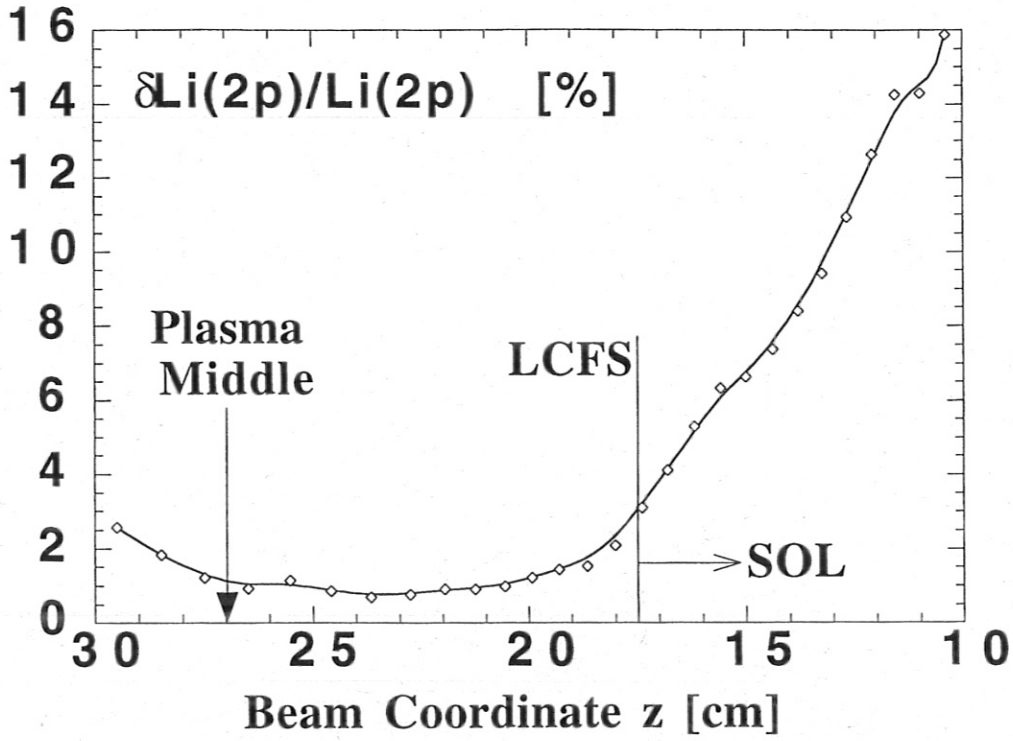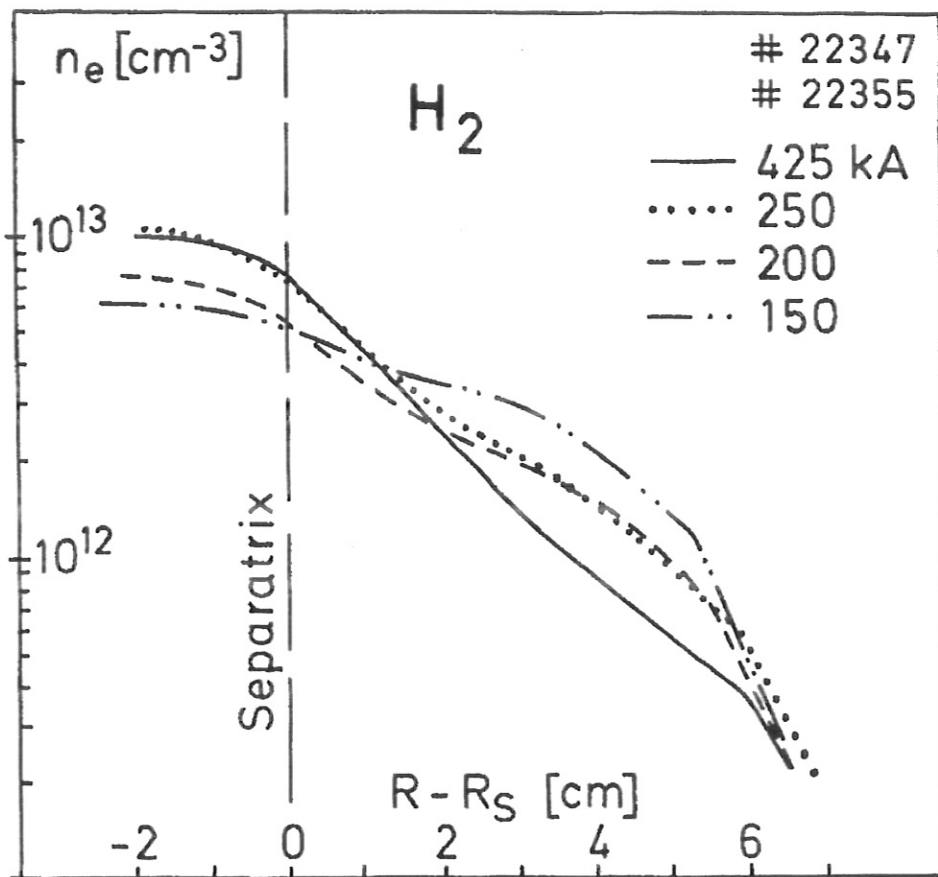
Fig. 18: Li(2p) profiles on W7-AS over a 20ms period.
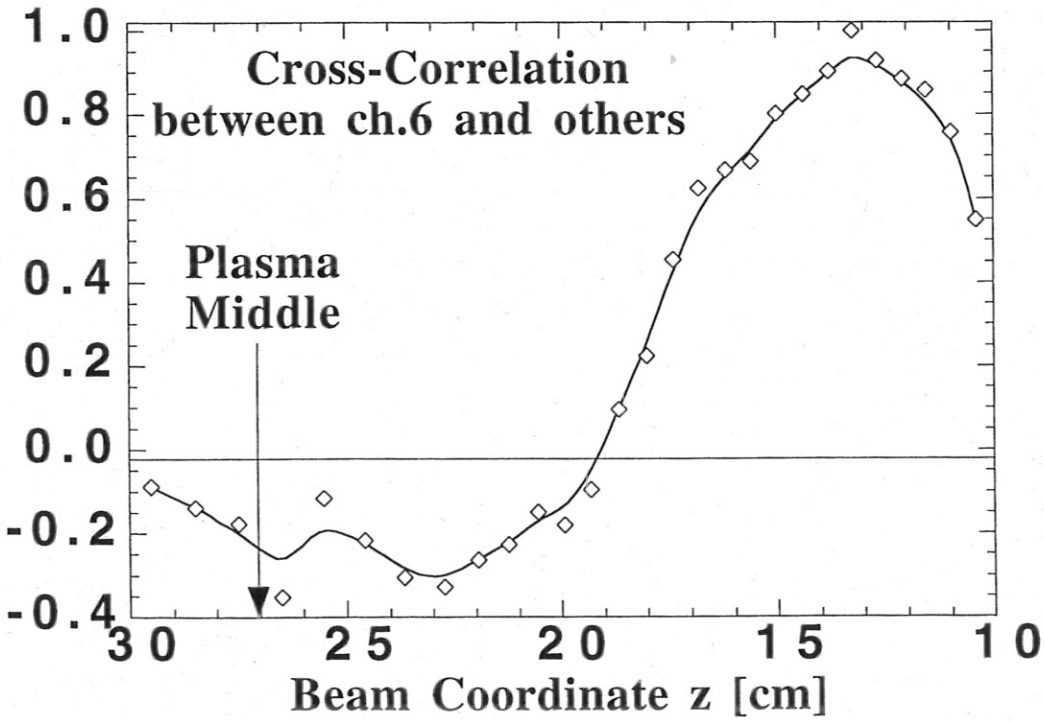
Fig. 19: Normalized Li(2p) fluctuation amplitude (top), cross correlation function between channel six (z~ 13.25 cm) and all others (bottom), vs. channel position.

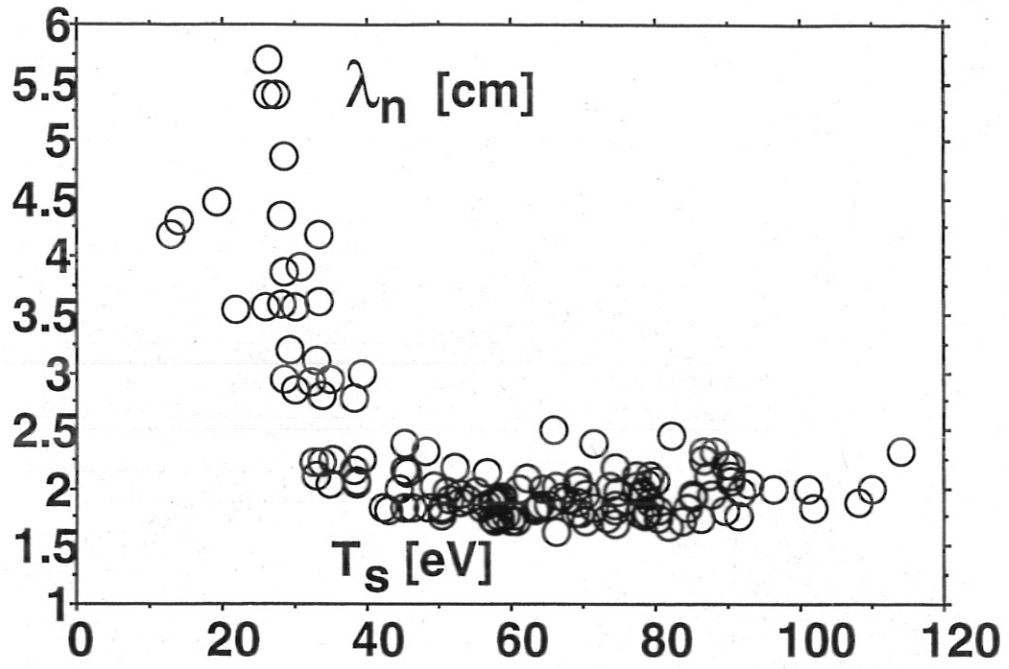**Fig. 20:** $n_e(R-R_S)$ profiles on ASDEX for four different currents.

Fig. 21: SOL density falloff lengths λ_n vs. T_e slightly inside the separatrix. **ASDEX**.
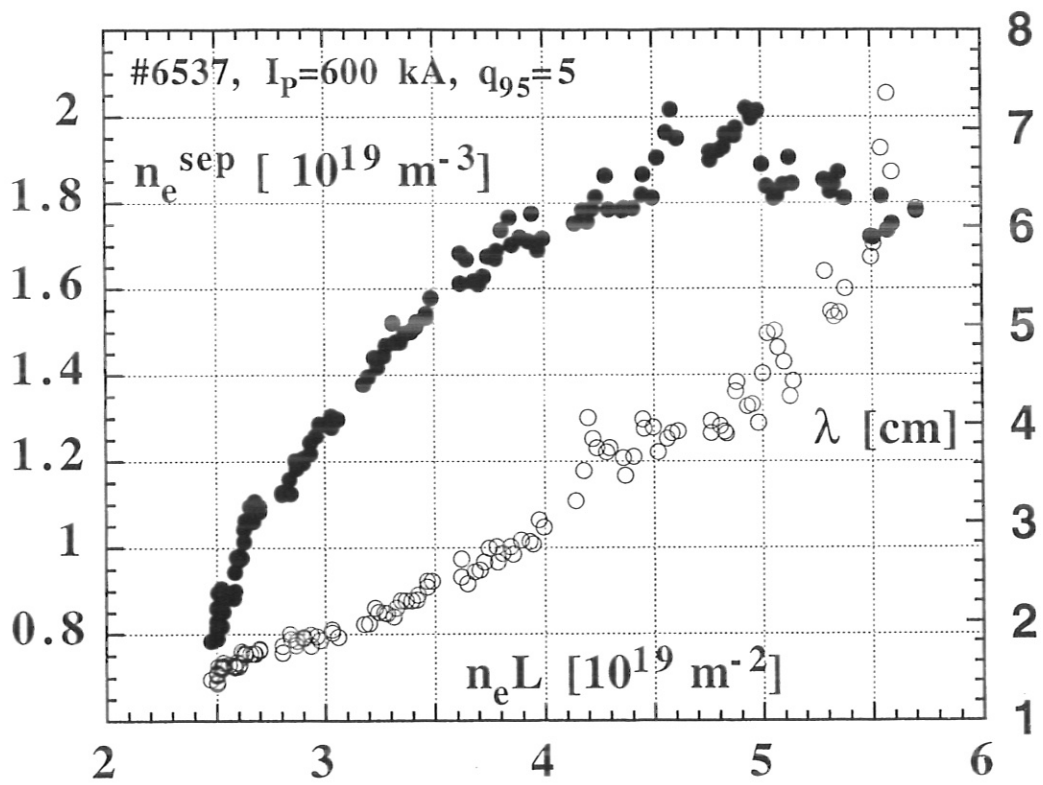
Fig. 22: n_e at the separatrix and SOL density falloff length λ_{ne} vs. $\overline{n_eL}$. ASDEX-Upgrade
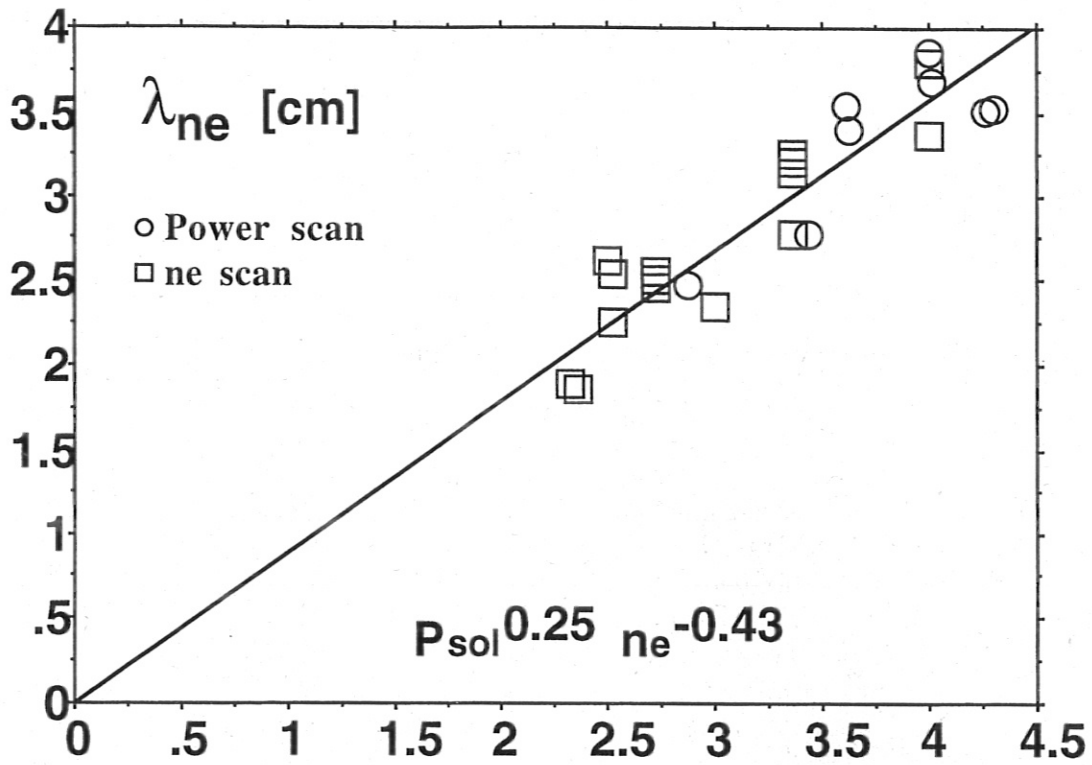
Fig. 23: Scaling of the SOL density falloff length λ_n for a density and power scan on **W7-AS**.